Antibody-Drug Conjugates

Zitierweise:
Internationale Ausgabe: doi.org/10.1002/anie.202302805
Deutsche Ausgabe: doi.org/10.1002/ange.202302805

Self-Assembled L–DNA Linkers for Rapid Construction of Multi-Specific Antibody-Drug Conjugates Library

Liujuan Zhou, Fan Yang, Zhaoshuai Bai, Xiaohui Zhou, Zhihai Zhang, Zhihang Li, Junyuan Gong, Junqi Yu, Liqiang Pan, Chan Cao,* and James J. Chou*

Abstract: One of the key challenges of improving clinical outcomes of antibody drug conjugates (ADCs) is overcoming cancer resistance to the antibody and/or drug components of ADCs, and hence the need for ADC platforms with high combinatory flexibility. Here, we introduce the use of self-assembled left-handed DNA (L–DNA) oligonucleotides to link combinatory single-domain antibodies and toxin payloads for tunable and adaptive delivery of ADCs. We demonstrate that the method allows convenient construction of a library of ADCs with multi-specific targeting, multi-specific payloads, and exact drug-antibody ratio. The newly constructed ADCs with L–DNA scaffold showed favorable properties of in vitro cell cytotoxicity and in vivo suppression and eradication of solid tumors. Collectively, our data suggest that the L–DNA based modular ADC (MADC) platform is a viable option for generating therapeutic ADCs and for potentially expanding ADC therapeutic window via multi-specificity.

Introduction

Past decade of cancer therapeutics development has witnessed a surge of antibody-drug conjugates (ADCs) with 13 ADCs approved by the U.S. Food and Drug Administration (FDA) for a variety of malignant cancers from acute myeloid leukemia (Gemtuzumab ozogamicin) to platinum-resistant ovarian cancer (Mirvetuximab soravtansine) and dozens more in pre-clinical and clinical development.[1] ADCs are generally perceived as targeted chemotherapy drugs and they all comprise three core components: an antibody that binds a tumor-associated antigen, a cytotoxic payload, and a connecting linker between them.[2] The canonical mechanism of action of ADC involves binding of the antibody (generally mAb in IgG format) to the target antigen, subsequent internalization of the ADC, breaking of the linker to release toxin payloads and, finally, endosomal escape of the payload to cytosol for inhibiting cell growth. The high specificity of an ADC to its target receptor, combined with controllable toxin release, result in ADCs having much less off target toxicity than their small molecule counterparts, thus providing larger therapeutic window for cancer patients.[3] Despite the benefits, development of ADC is still confronted with technical challenges of production such as heterogeneous drug-antibody ratio (DAR)[4] and linker instability,[5] as well as the fundamental issue of resistance.[6]

In recent years, progress in protein engineering and synthetic chemistry of new linkers and toxins have paved the way to overcome the above technical challenges. Homogeneous ADCs with a DAR of 2 have repeatedly demonstrated superior therapeutic performance compared to their heterogeneous counterparts.[7] Thus, a wide range of methods have been developed for achieving uniform DAR, exemplified by the THIOMAB method of engineering cysteines into antibody for site-selective payload conjugation[8] and enzymatic methods such as transglutaminase (TGase)-mediated transamidation for selective conjugation at the γ-amyl group of glutamine residue and the ε-amino group of lysine.[9] To improve payload delivery efficiency, innovative linkers have been developed to promote selective release of cytotoxic agents by exploiting

[*] L. Zhou, Z. Bai, Z. Li, J. Yu
Assembly Medicine, LLC
Shanghai 201203 (China)
Prof. Dr. F. Yang, Z. Zhang
Artificial Intelligence and Bioinformation Cognition Laboratory, School of Communications and Electronics, Jiangxi Science and Technology Normal University
Nanchang, 330029 (China)
E-mail: kooyang@aliyun.com
X. Zhou, J. Gong, Prof. Dr. C. Cao
State Key Laboratory of Elemento-Organic Chemistry and Frontiers Science Center for New Organic Matter, College of Chemistry, Nankai University
Tianjin, 300071 (China)
E-mail: chancao@nankai.edu.cn
Prof. Dr. L. Pan
Institute of Drug Metabolism and Pharmaceutical Analysis and Zhejiang Province Key Laboratory of Anti-cancer Drug Research, College of Pharmaceutical Sciences, Zhejiang University
Hangzhou, 310058 (China)
Prof. Dr. J. J. Chou
Interdisciplinary Research Center on Biology and Chemistry, Shanghai Institute of Organic Chemistry, Chinese Academy of Sciences
Shanghai, 201203 (China)

specific hallmarks of the tumor microenvironment such as enzyme-activable Val-Cit linker,[10] pH-sensitive spiro-orthoester linker,[11] near-infrared light-sensitive cyanine linker,[12] or to improve the solubility by employing polyethylene glycol (PEG) spacer or negatively charged sulfonate groups.[13] Apart from bioconjugation methods, novel payloads have also been developed to exert maximal cytotoxic effects at a minimal concentration such as the RNA polymerase II inhibitor α-amanitin, tubulin inhibitor cryptophycins, RNA spliceosome inhibitor spliceostatins and thailanstatins.[14]

Despite the ever-growing repertoire of ADC tools and greatly improved ADC anti-tumor efficacy, frequent occurrence of drug resistance unfortunately has been one of the major factors limiting ADC clinical success. Mechanism conferring resistance can be multifaceted, including antigen-related resistance, poor internalization, and resistance to payload.[6] It has been shown, for the HER2 treatment route, that resistance to ADCs takes longer to develop than resistance to their constituent mAb or drug.[15] For example, mutations downstream of the HER2 signaling pathway would not prevent the payloads from accumulating and destroying the cells. ADCs are, however, still subject to resistance, like most cancer drugs. One source of resistance comes from changes (mutations or expression level) in cell surface receptors. Antigen down-regulation, shedding of receptor ectodomain or its masking by extracellular matrix components have been described as mechanism of resistance of ADCs such as trastuzumab emtansine (T-DM1)[16] and Brentuximab vedotin.[17] Another culprit is the multi-drug resistance pumps (MDRPs) that actively clear the toxins released by ADC. For example, increased expression of MDRP or reduced MDRP selectivity can increase the rate of developing resistance to ADCs. A study using trastuzumab emtansine (T-DM1)-resistant breast cancer cell line (KPL-4) showed that upregulation of MDR1 contributes to resistance and the T-DM1 resistance of KPL-4 can be reversed by treatment with an inhibitor of MDR1.[18]

An obvious solution to overcome resistance is engineering ADCs capable of targeting multiple antigen epitopes and/or carrying multiple toxins. For example, a dual-payload ADC with MMAE and MMAF has shown greater treatment effect and reduced drug resistance in xenograft mouse models with intratumor HER2 heterogeneity.[19] A bispecific ADC with biparatopic HER2-targeting has demonstrated strong therapeutic activity in breast cancer models representing T-DM1 resistant and ineligible patient populations.[20] To harness the potential of multi-specific ADCs, several creative methods have been developed in the last few years,[20,21] and the most prominent example is using bio-orthogonal click chemistry, branched ADC linker and chemoenzymatic conjugation to achieve dual-drug ADCs with defined DARs.[19]

Inspired by the above exploratory applications of multi-specific ADCs as well as earlier studies that exploited the property of oligonucleotide base pairing to link antibody to other antibodies or drugs,[22] we sought to develop a modular platform for rapid construction of multi-specific ADCs of all varieties for testing therapeutic hypotheses. The high modularity is based on left-handed DNAs (L–DNAs) that are optimized to self-assemble in a precise and homogeneous manner. We showed that a set of modular antibody-(L–DNA)-drug conjugates can rapidly and accurately assemble to form a library of multi-specific ADCs with bispecific targeting, bispecific payload, and tunable exact DAR suitable for high-throughput functional screening. Further, these ADCs with L–DNA scaffold exhibited good therapeutic efficacy and safety profiles in vivo, making them potential drug candidates.

Results and Discussion

Design of a modular ADC platform

For designing a modular ADC (MADC) platform with high combinatory flexibility, we prioritized on three criteria. One is the requirement for antibody and payload modules to self-assemble accurately such that homogeneous ADC complexes with exact and tunable drug-antibody and drug-drug ratios can be easily achieved. Another requirement is that the assembled ADC complex is compatible with known ADC mechanism such as efficient internalization upon antigen engagement and payload release in endosomes. Finally, the assembled ADC complexes need to be stable and have low immunogenicity in vivo. Taking all above into consideration, we have chosen L–DNA oligonucleotides to be the linker that can be conjugated to antibody and/or drug to generate an inventory of basic assembly units. By designing the L–DNA sequences such that they specifically oligomerize (e.g., to tetramer or pentamer) via base pairing, these basic units can spontaneously form homogeneous ADCs in solution with desired targeting and cytotoxic features (Figure 1). L–DNA has the base pairing property of D-DNA but does not occur naturally and is thus not a substrate of any nucleases.[22b,23] Nor it is recognized by receptors of the innate immunity.[24] Moreover, the negatively charged L–DNA could provide additional benefit of reducing ADC hydrophobicity, as previous in vivo studies have demonstrated an inverse correlation between apparent hydrophobicity of ADC and therapeutic index.[25] On the side of antibody, we have chosen the single-domain antibodies (sdAbs) for targeting antigens as they are small, structurally stable, and convenient for secreted expression by yeast and purification. The overall approach of MADC is building an inventory of sdAb-(L–DNA) and (L–DNA)-drug units for separate storage, which can be used to generate a combinatorial library of ADCs for functional screen and potentially therapeutic application.

Computer aided optimization of L–DNA sequences for accurate self-assembly

The success of MADC depends strongly on the ability of L–DNA oligonucleotides to assemble accurately under ambient temperature (20–30 °C). The L–DNAs need to be sufficiently long to form highly stable complex with T_m

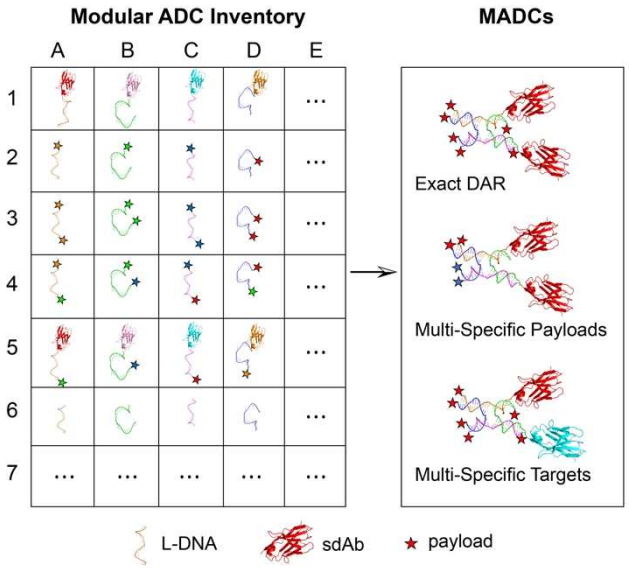

Figure 1. Design concept of the modular ADC platform. Different modular ADC units are prepared and stored separately (*left*), which can self-assemble into various MADC formats for functional screening and therapeutic application (*right*).

$>50\,^{\circ}C$, but the assembled L–DNA complex should be no larger than 50 kDa to allow for efficient renal clearance.[26] A compromised length of 30–34 basepairs (bps) per oligonucleotide was thus used for assembling tetramer. For the tetramer with four double-stranded arms, we adopted the classic Holliday junction structure but enforced top-down and left-right mirror symmetry to simplify sequence design (Figure 2a). The key challenge, however, was to optimize the sequences to maximize the intended pairing while minimizing the off target pairing. This is particularly important for spontaneous assembly into the desired oligomer at ambient temperature without unwanted by-products. We have thus developed computer algorithm for sequence optimization.

Briefly, an interaction energy matrix was constructed containing free energy (ΔG) values of all possible double-stranded pairing. Taking the tetramer for example, each of the four chains has two variable regions to pair with different chains. The matrix $\mathbf{M}_{ij}$ would be 8×8 in which the matrix elements are ΔG_{ij} of base pairing between segments *i* and *j*. The goal of sequence optimization was to maximize ΔG of non-specific (unwanted) pairing while keeping the intended pairing segments fully paired. As such, we defined the energy function for non-specific pairing as

$$E^{NS} = \sum_{i=1}^{n}\sum_{j=1}^{n} \Delta G_{ij}^{NS},\ n = 8,$$

where $\Delta G_{ij}^{NS} = 0$ for specific (intended) base pairing between segments *i* and *j* and employed the Metropolis Monti Carlo simulation with Simulated Annealing (MMCSSA) to minimize E^{NS} via iterative mutagenesis (Figure 2b, S1). Electrophoresis analysis of the optimized tetramer sequences showed significantly more homogeneous assembly than those manually designed by us (Figure 2c; details in Supplementary Methods). Similar optimization approach should be applicable to higher assemblies such as pentamers and hexamers.

Implementation of MADC

Chemical conjugation involving L–DNA under physiological buffer conditions is essential for the implementation of MADC. For conjugation with sdAb, a free cysteine was appended to the sdAb C-terminus (designated sdAb-Cys) and 5′-amino-modifier C6 linker was added to the 5′ end of L–DNA to introduce a primary amine group (designated 5′-amino-L–DNA). The 5′-amino-L–DNA and sdAb-Cys can then be conjugated with a PEGylated SMCC bifunctional linker (Figure 3a). We tested the above synthetic scheme on a previously reported sdAb that binds to the ectodomain IV of human epidermal growth factor receptor 2 ($HER2^{IV}$)[27] and found that conjugation efficiency was high, reaching more than 95 % at 1:2 ratio of sdAb to L–DNA (Figure 3a). Similar conjugation efficiency was observed for other sdAbs such as those targeting the human serum albumin (HSA)[28] and HER2 ectodomain II[29] (Figure S2). For the sdAb-oligos in Table S1, the yield in our laboratory was 40–60 % (yield = output quantity of sdAb-oligo (mole)/input quantity of sdAb (mole)) for achieving >99 % purity.

For conjugation with payload, homo-bifunctional L–DNA with 5′- and 3′- amino modifications and hetero-bifunctional L–DNA with 5′-amino and 3′-thiol modifications were synthesized. The 5′-amino ends can conjugate to payloads with activated ester linker such as OSu-Glu-vc-PAB-MMAE (Figure 3b) and SPDB-DM4 (Figure S3), while the 3′-thiol ends can conjugate to payloads with maleimide group such as MC-vc-PAB-Duocarmycin and MC-vc-PAB-MMAF (Figure 3c). We found that L–DNAs performed well in both homo- and hetero- bifunctional conjugation with the known ADC payloads. In the case of OSu-Glu-vc-PAB-MMAE, for example, the reaction efficiency reached almost 100 % in one step at 1:70 molar ratio of L–DNA to the payload (Figure 3b). The hetero-bifunctional conjugation was achieved in sequential reactions, first between L–DNA 5′-amino group and OSu-Glu-vc-PAB-MMAE, and then between the 3′-thiol group of the same L–DNA and MC-vc-PAB-Duocarmycin. The reaction efficiency also reached almost 100 % at 1:50 molar ratio of L–DNA to OSu-Glu-vc-PAB-MMAE or 1:20 molar ratio of L–DNA to MC-vc-PAB-Duocarmycin (Figure 3c). Moreover, the hetero-bifunctional L–DNA can be applied to conjugate sdAb and payload with 5′-amino and 3′-Cys ends, respectively (Figure 3d). In our laboratory, the yield was 75–95 % for the toxin-oligos in Table S1 (yield = output quantity of toxin-oligo (mole)/input quantity of oligo (mole)) for achieving >99 % purity.

The above conjugation results indicate that L–DNA is highly amenable to bioconjugation with sdAb and a variety forms of ADC toxins. Using the conjugation schemes, we constructed an inventory of basic units for four-arm MADC

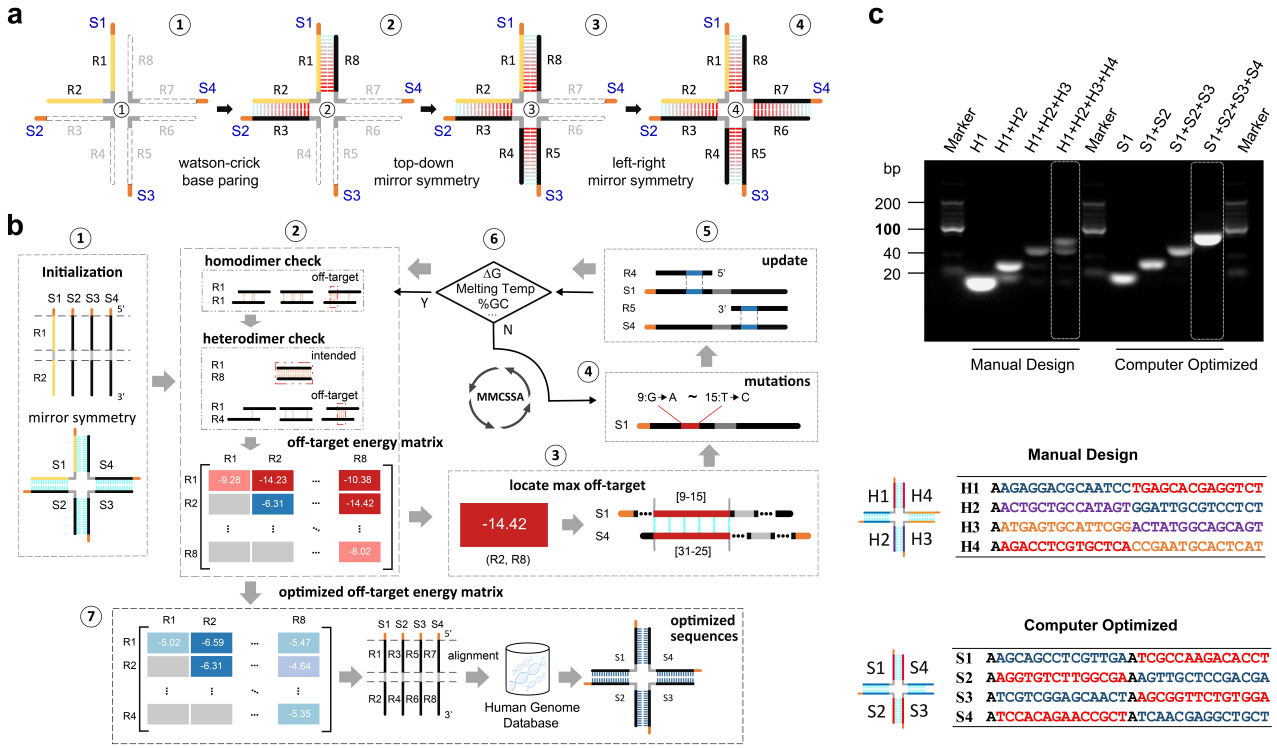

Figure 2. Computer aided optimization of L–DNA sequences for accurate self-assembly. (**a**) Design of self-assembled tetramer with mirror symmetry DNA sequences. From *left to right*: (1) sequence initialization of the first DNA chain (S1) comprising two regions (R1 and R2) for inter-chain pairing; (2) sequence generation of R3 of S2 and R8 of S4 by complementary base pairing; (3) generation of R4 of S2 and R5 of S3 based on top-down mirror symmetry; (4) generation of R6 of S3 and R7 of S4 based on left-right mirror symmetry. The orange and grey regions of S1–S4 represent spacers comprising 1–3 bases. (**b**) Flow diagram of sequence optimization using the Metropolis Monti Carlo simulation with simulated annealing (MMCSSA; Methods). (1) Sequence initialization: generate S1 with minimal unwanted homodimerization and initialize S2–S4 sequences based on mirror symmetry as in (a). (2) Find off-target base pairing between the same and different chains; calculate ΔG of unwanted pairing and construct the off-target energy matrix. (3) Identify the region with the smallest ΔG for repair. (4) Random mutagenesis of the repair region. (5) Update the tetramer sequences based on the mutations. (6) Evaluate the new sequences for meeting the Metropolis criterion as well as target T_m and GC content; repeat 2–5 until the criteria are met. (7) The final optimized off-target energy matrices and corresponding sequences are subject to a final selection based on the desired T_m and GC content, as well as low similarity with human DNA fragments. (**c**) *Upper*: agarose gel electrophoresis analysis of manually designed tetramer based on Holiday junction sequences and computer optimized tetramer based on mirror symmetry scaffold. *Lower*: the non-optimized sequences (H1-H4) and computer-optimized sequences (S1–S4) used in the gel analysis. The tetramers were assembled by mixing four chains at 25 °C for 1 min before gel electrophoresis.

assembly including, for example, anti-HER2^{IV}-S3, anti-HER2^{II}-S4, anti-HSA-S4-MMAE, MMAE-S1, and MMAE-S2-MMAE, where S1–S4 represent the four L–DNAs that assemble to form tetramer (full list in Table S1, Figure S3–S4). These units constitute the basis set of MADCs investigated in this study.

Therapeutic potential of MADC: proof-of-principle

Equipped with the MADC inventory in Table S1, we assembled anti-HER2 MADCs with defined DAR and evaluated their therapeutic potential with in vitro cytotoxicity, in vitro cell internalization, and in vivo tumor eradication. For example, using the modules anti-HER2^{IV}-S3 (for cancer targeting), anti-HSA-S4 (for in vivo stability), MMAE-S1-MMAE and MMAE-S2-MMAE (as toxin payloads), we could rapidly assemble an anti-HER2 MADC with a DAR of 4 (Drug A) by mixing the four modules at equimolar ratio (Figure 4a). Target binding affinities of the assembled MADC were confirmed by Bio-Layer Interferometry (BLI), which showed dissociation constants (K_D) of 3.02 and 15.03 nM for HER2^{IV} and HSA, respectively (Figure S5).

We next evaluated in vitro cytotoxicity of the MADC using the breast cancer cell line HCC1954. The similarly assembled tetramers without sdAb (Drug B) or without payload (Drug C) were used as negative controls. Moreover, the FDA-approved anti-HER2 ADC, named T-DM1, was used for head-to-head comparison. T-DM1 with an average DAR of ≈3.5, made by conjugating the toxin maytansinoid (DM1) to the anti-HER2^{IV} IgG (trastuzumab).[30] The cells were treated with the above test articles in parallel. We found that Drug A and T-DM1 showed similar cytotoxic efficacy with EC_{50} of 0.16 ± 0.01 and 0.15 ± 0.01 nM (Figure 4b, left), although the HER2 binding affinity of Drug A

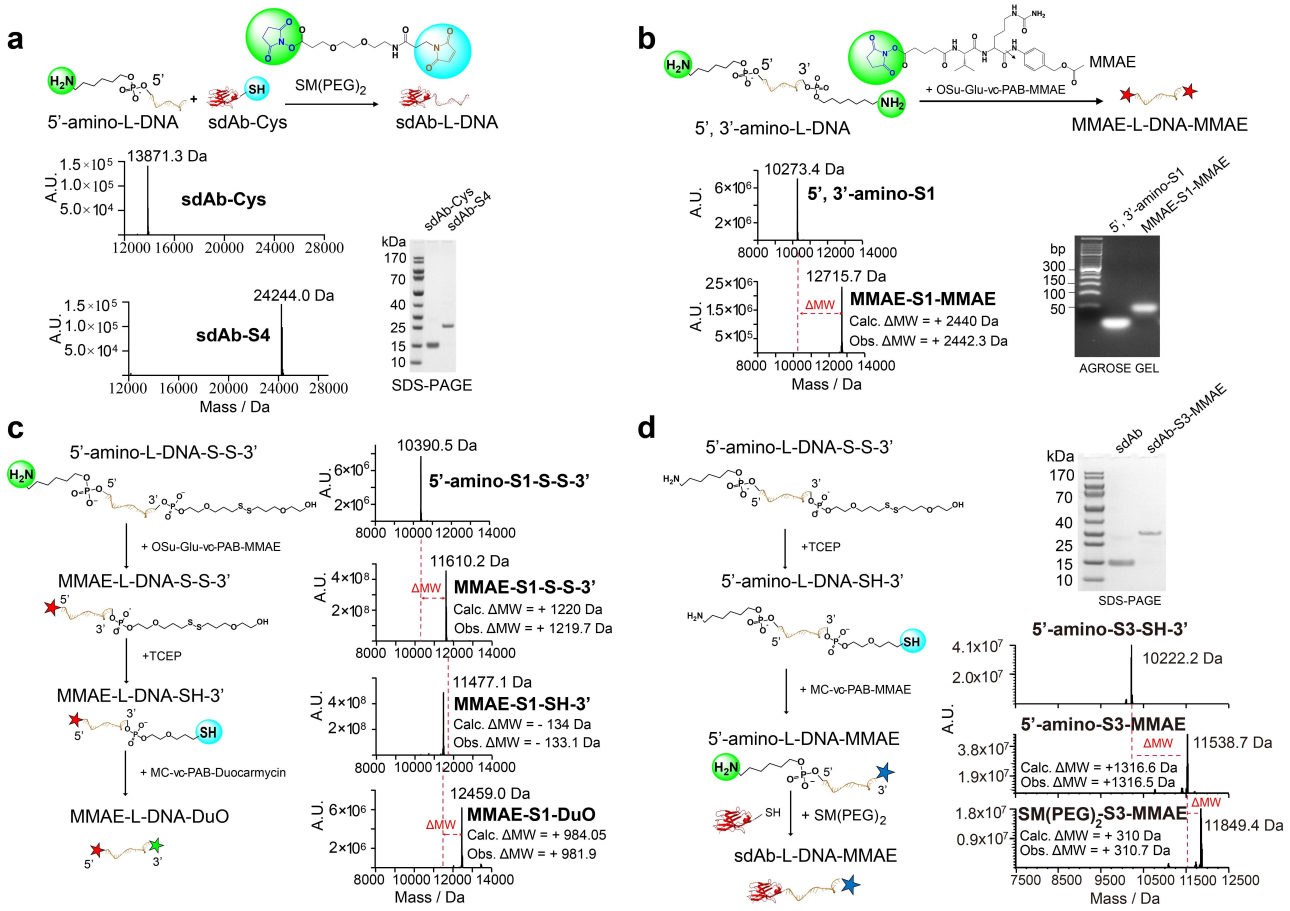

Figure 3. Bioconjugation chemistry for MADC implementation. The reactions used include (1) between primary amine and NHS moieties (highlighted in green) and (2) between thiol and maleimide moieties (highlighted in blue). The conjugation efficiency was determined with ESI Mass Spectrum and gel electrophoresis. (**a**) Conjugation of 5′-amino-L–DNA to the sdAb-Cys via PEGylated SMCC linker to generate sdAb-L-DNA. (**b**) Conjugation of 5′, 3′-amino-L–DNA to NHS-MMAE to achieve homo-bipayload L–DNA, MMAE-L-DNA-MMAE. (**c**) Conjugation of 5′-amino-L–DNA-S-S-3′ first to NHS-MMAE and then to maleimide-Duocarmycin to generate hetero-bipayload L–DNA, MMAE-L-DNA-Duocarmycin. (**d**) Conjugation of 5′-amino-L–DNA-S-S-3′ first to maleimide-MMAE and then to sdAb-Cys (via $SM(PEG)_2$) to generate sdAb/payload hetero-bifunctional L–DNA, sdAb-L-DNA-MMAE.

(K_D = 3.02 nM) is ≈30-folds lower than that of T-DM1 (K_D = 0.1 nM).[31] The same MMAE complex without targeting ability (Drug B) showed about 40-folds lower potency (EC_{50} = 6.3 ± 1.2 nM) and the drug complex without MMAE (Drug C) showed no cytotoxic activity (Figure 4b, left). We also performed a parallel experiments to test the effect of Drug A on $HER2^+$ HCC1954 and $HER2^-$ MCF-7 cell lines. As expected, drug A caused strong killing of $HER2^+$ HCC1954 but did not affect the growth of $HER2^-$ MCF-7 (Figure S6). These results indicate that the anti-HER2 MADC has similar antigen-dependent killing of cancer cells as T-DM1 and that the L–DNA linkers could not have contributed to cell killing independent of the payload.

To validate the antigen-dependent endocytosis mechanism of MADC, we performed cell internalization assay for Drugs A, B and T-DM1. For this assay, Drugs A and B were assembled in the same format as in the cytotoxicity assay except the toxin MMAE was replaced with the pHrodo™ Red probe, which is a pH-sensitive probe for reporting pH change along the endocytic pathway. The newly assembled drugs were designated A-pHrodo and B-pHrodo, respectively. Similarly, T-DM1-pHrodo was prepared by replacing DM1 toxin with pHrodo (Methods). The HCC1954 cells were treated with A-pHrodo, B-pHrodo, and T-DM1-pHrodo in parallel, resulting in very different internalization properties (Figure 4b, right). For A-pHrodo, the fluorescent signal increased rapidly with incubation time, reaching saturated intensity after 2.5 h. The pHrodo signal of the benchmark T-DM1, however, increased much more slowly, reaching the maximum intensity after 20 h. As expected of the negative control B-pHrodo, no increase in pHrodo signal was detected. The results indicate that the molecular format of MADC is compatible with rapid receptor-binding mediated internalization.

To further explore the tunability of MADC efficacy, we performed efficacy vs. DAR study of the anti-HER2 MADC using a variety of cancer cell lines. In a tetrameric framework, anti-HER2 MADCs with DARs of 0, 2, 4, and 6 (designated Drugs C, D, A and E in Table S2) were assembled with several basic units from Table S1. For

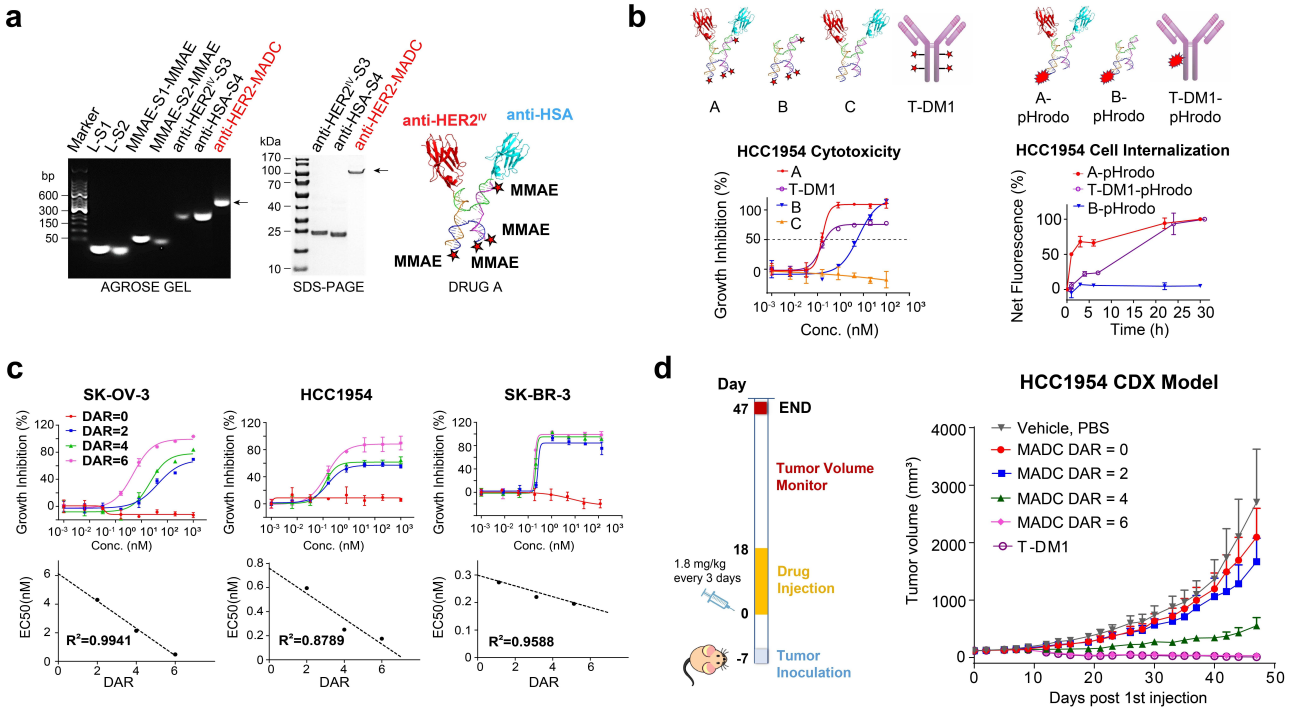

Figure 4. Therapeutic potential MADC. (**a**) Agarose gel electrophoresis (*left*) and SDS-PAGE (*middle*) analysis of anti-HER2 MADC (Drug A, assembled complex marked by arrow); schematic of the drug assembly is in *right* panel. (**b**) *Left*: Effect of treating the HCC1954 cell with anti-HER2 MADC, anti-HER2 MADC without sdAb or payload, and T-DM1 at various concentration; cell viability was measured by Cell Titer-Glo luminescent cell viability assay after 72 h incubation. *Right*: Internalization kinetics of pHrodo-labeled anti-HER2 MADC without payload, L–DNA scaffold, as well as Trastuzumab (see schematic in the figure) in HCC1954 cells; drug internalization was reported as the net fluorescent change due to decreased pH. (**c**) Effect of treating SK-OV-3, HCC1954, and SK-BR-3 cells with anti-HER2 MADC with different DARs from 0 to 6 at various concentration. Cell viability was measured by Cell Titer-Glo luminescent cell viability assay after 72 h incubation. (**d**) In vivo antitumor activity of MADCs with different DAR in the HER2$^+$ HCC1954 murine xenograft model. HCC1954 cells were implanted subcutaneously into BALB/c nude mice ($n=6$ per group) and treated via intravenous injection with MADCs with DARs from 0 to 6 as well as PBS and T-DM1. *Left*: The drugs were administered every 3 days for 7 times (1.8 mg kg^{-1} per injection). *Right*: Tumor size was monitored 3 times per week for 47 days.

example, the MADC with a DAR of 6 was assembled with MMAE-S1-MMAE, MMAE-S2-MMAE, anti-HER2^{IV}-S3-MMAE, and anti-HSA-S4-MMAE (Figure S7). The three cell lines used included the ovarian cancer cell SK-OV-3, the breast cancer cell HCC1954, and the HER2 high expression breast cell SK-BR-3. The cells were treated with the above anti-HER2 MMAE MADCs with different DARs in parallel. We found that for all three cell lines, the MADC framework exhibited a linear correlation between cytotoxic efficacy and DAR (Figure 4c; Table S3).

We then tested in vivo tumor suppression by the above anti-HER2 MADCs with different DARs using the subcutaneous HER2$^+$ HCC1954 murine xenograft model. After the tumor reached 100–200 mm^3, MADCs with DAR of 0, 2, 4, and 6 were administered intravenously every 3 days for 7 times with the dosage of 1.8 mg kg^{-1} (Figure 4d, left). In addition, PBS (negative control) and T-DM1 (positive control) were administered in the same way. Each study group comprised 6 mice ($n=6$). Consistent with the in vitro assays, the in vivo results show a strong DAR-dependent tumor killing with larger DAR yielding smaller EC_{50} (Figure 4d, right). At the end of study (Day 47), tumor growth inhibition (TGI) of various drug groups were 23.58 % (DAR = 0), 40.15 % (DAR = 2), 83.21 % (DAR = 4), 103.30 % (DAR = 6), and 104.14 % (T-DM1) relative to the PBS group (Figure S8a; Table S4). Moreover, compared to the PBS group, no significant changes in body weight were observed during treatment with different DARs (Figure S8b), suggesting that the MADCs did not induce significant systemic toxicity. To further investigate potential hepatotoxicity of MADC drug, healthy Sprague-Dawley (SD) rats were injected intravenously with low (0.5 mg kg^{-1}) or high (5 mg kg^{-1}) dose of MADC Drug E (DAR = 6) and with PBS as negative control ($n=3$ per group). The blood chemistry parameters aminotransferase (AST) and alanine aminotransferase (ALT) associated with liver function were measured on Days 5 and 14. These parameters were all within normal ranges (Figure S9), suggesting that the MADCs did not induce significant hepatotoxicity. Overall, the results demonstrate that the MADC platform can be conveniently used for tuning exact DAR. In this case, the MADC with a DAR of 6 could completely suppress tumor growth.

Since L–DNA is resistant to nucleases, we also investigated whether the tetrameric L–DNA linker can be cleared via the renal pathway once the MADC is degraded. We assembled the L–DNA tetramer in which the S1 strand was conjugated with the near-IR fluorescent probe Cy5.5 at the

5′ end (Figure S10a). Eight groups of BALB/c mice ($n=3$ per group) were injected intravenously with the L–DNA-Cy5.5 tetramer at a dose of 2.64 mg kg^{-1} for imaging at 8 different time points (t = 0.5, 2, 4, 8, 24, 48, 96 and 168 h). In parallel, control mice were injected with PBS. We found that the Cy5.5 labeled L–DNA reached systemic distribution within 0.5 h (Figure S10b). Then in 0–4 h and 4–8 h, the L–DNA was largely eliminated via renal clearance as significant amount of intact L–DNA tetramers were detected in urine (Figure S10b). Based on the concentration vs. HPLC peak area calibration curve (Figure S10c), the L–DNA concentration in urine was quantified as 69.1 ng μl^{-1} for 0–4 h and 27.8 ng μl^{-1} for 4–8 h. With ventral body imaging, we found that ≈80 % of the L–DNA tetramer was cleared within 24 h (Figure S11).

Screen of dual target/payload combinations with MADC

Drug resistance has been one of the major factors limiting ADC clinical success, and cells can evade ADC activity by multiple mechanisms, such as heterogeneous antigen expression, attenuated ADC internalization, or resistance to payload. Here, we assess the potential of the MADC platform for screening for multi-specific targeting and multi-specific payload. The combinatorial flexibility of MADC allowed for convenient construction of a library of ADCs with different targeting valency, multi-specific toxin, and multi-specific targeting (Figure 5a).

For comparing different HER2 targeting valency, we prepared MADCs with 0, 1, or 2 anti-HER2^{IV} sdAbs, all with MMAE (DAR = 4) and one anti-HSA sdAb (Figure 5b). The MADCs with mono- or bivalent HER2 targeting (Drug A or G) showed similar and strong cytotoxic potency with relative EC_{50} of 0.16 ± 0.01 and 0.13 ± 0.02 nM, whereas the MADC without anti-HER2 sdAb (Drug F) showed about 40-folds lower potency (EC_{50} = 5.7 ± 1.3 nM) (Figure 5b).

For exploring with multi-specific toxin screening, we first prepared an anti-HER2^{IV} MMAE MADC with DAR = 2 and tested its efficacy against 4 different HER2^{+} cell lines including SK-BR-3, HCC1954, SK-OV-3, and JIMT-1. We found that, out of the 4 cell lines, SK-BR-3 and HCC1954 responded well to the mono-specific toxin drug whereas the Trastuzumab resistant cell line JIMT-1 and human ovarian cancer cell line SK-OV-3 showed poor growth inhibition (Figure 5c). We then treated the non-responsive cell lines (JIMT-1 and SK-OV-3) with MADCs with the same anti-HER2^{IV} MMAE MADC except one of the two MMAEs was replaced by DM4 or MMAF. The above toxins have different working mechanism. MMAE is a cell membrane permeable toxin with bystander

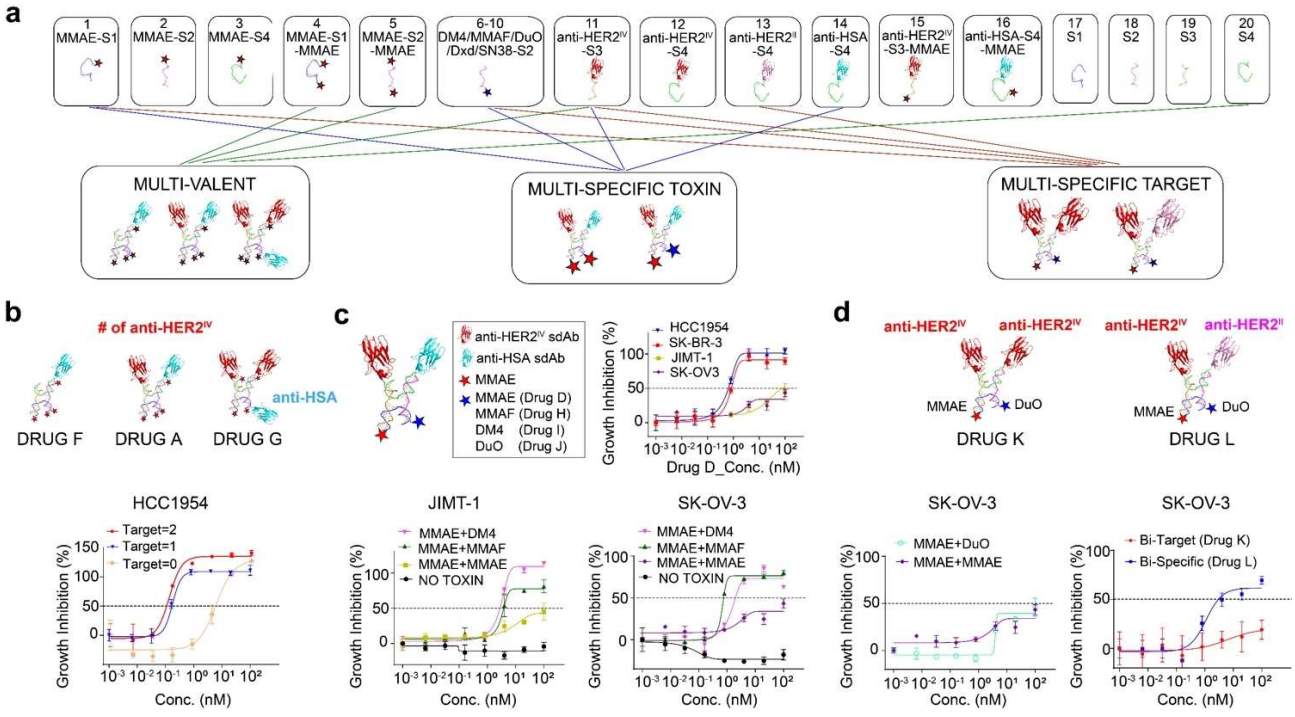

Figure 5. (**a**) Schematic illustration of preparing MADCs with multi-valent targeting, multi-specific toxin, or multi-specific targeting from an inventory of MADC units. (**b**) *Upper*: Schematics of MADCs containing 4 MMAEs, 1 anti-HSA sdAb, and 0, 1, or 2 anti-HER2^{IV} sdAbs. *Lower*: dose-response cytotoxic effect of the drugs on HCC1954 cells. (**c**) *Upper left*: Schematics of MADCs containing 1 anti- HER2^{IV} sdAb, 1 anti-HSA sdAb, and 1 MMAE in combination with 1 MMAE, MMAF, DM4, or DuO toxin. *Upper right*: dose-response growth inhibition of the MADC with 2 MMAEs on 4 different HER2^{+} cell lines including HCC1954, SK-BR-3, JIMT-1, and SK-OV-3. *Lower panels*: The cell lines JIMT-1 and SK-OV-3 not responsive to 2 MMAEs were treated with different toxin combinations including MMAE + DM4 and MMAE + MMAF. (**d**) *Upper*: Schematics of MADC containing monospecific targeting against HER2^{IV} and dual payloads (MMAE + DuO) and containing bispecific targeting against HER2^{IV} and HER2^{II} and the same dual payloads. *Lower*: Comparing dose-response cytotoxic effects of the mono- and bi- specific targeting. The cell viability in (b–d) was measured using the Cell Counting-Lite 2.0 Luminescent Cell Viability Assay after 72 h incubation.

effect, and it is a good substrate of the drug efflux pump. MMAF is a cell membrane-impermeable toxin without bystander effect and cannot be pumped out once delivered to the intracellular compartment. DM4 suppresses microtubule dynamics and causes cell cycle arrest in the G2/M phase. We found that MADCs with MMAE + MMAF or MMAE + DM4 exhibited significantly higher cytotoxicity than $(MMAE)_2$ (Figure 5c). Compared to $(MMAE)_2$, MMAE + MMAF improved cell inhibition from 43 % to 78 % for JIMT-1 and 34 % to 76 % for SK-OV-3, and MMAE + DM4 improved cell inhibition from 43 % to ≈100 % for JIMT-1 and 34 % to 73 % for SK-OV-3.

Finally, we tested MADCs with multi-specific targeting and multi-specific toxins. In this case, we prepared a MADC having bivalent targeting (2 anti-HER^{IV} sdAbs) and bi-specific toxins including one MMAE and one Duocarmycin (DuO), which is a potent toxin capable of inducing a sequence-selective alkylation of duplex DNA. However, this drug did not show obvious improvement over $(MMAE)_2$ for the SK-OV-3 cell line (Figure 5d, left). We then further introduced bispecific targeting functionality into the bispecific toxin MADC by replacing one of the two anti-$HER2^{IV}$ sdAbs by an anti-$HER2^{II}$ sdAb. The new bispecific targeting/toxin MADC showed significant improvement from 20 % to 62 % for SK-OV-3 cell line (Figure 5d, right). The above experiments show that combinatorial screening of multi-specific targeting/toxin has the potential of drastically improving the efficacy of ADC therapeutics while demonstrating that the MADC platform allows convenient construction of a library of MADCs with multi-specific targeting and multi-specific payloads.

Conclusion

We have shown that the MADC platform offers the combinatorial flexibility to screen for optimal target and payload combinations for the management of emerging ADC resistance while having the potential of becoming viable therapeutic agents themselves. The key advantage of the MADC approach is that given an established inventory of antibody and toxin units, a large variety of ADCs with distinct cancer targeting and killing properties can be prepared by simple mixing of the units in solution. Previous studies implementing self-assembled multi-specific antibodies have alluded to the power of modularity in screening of antibody combinations for T cell redirected killing of cancer cells.[22a,b] The current study demonstrates that with the use of a library comprising 3 different sdAbs and 4 different toxins, we were able to rapidly test the in vitro cytotoxicity of 12 different ADCs. Such flexibility would afford large scale screens for ADCs with multi-specific targeting and payload potential. Of note, the target and toxin diversity in clinical trials have increased rapidly in the past 10 years. Out of the 82 novel ADCs registered with clinicaltrials.gov for cancer patients (access date 15 May 2021), there are approximately 40 different targets and over 20 different payloads such as tubulin disruptors, DNA damaging agents, topoisomerase inhibitors, RNA polymerase inhibitors, and toll-like receptor agonists.[32] The MADC platform offers an efficient solution for harnessing the potential of the ever-growing ADC target and toxin inventory for overcoming drug resistance.

In addition to being a screening platform, our study suggests that the molecular format of MADC also has strong potential of becoming therapeutic drug itself. First, the anti-HER2 MADC with a DAR of 6 has essentially the same in vivo tumor suppression activity as T-DM1 with DAR ≈4 (Figure 4d). Since the HER2 binding of MADC is monovalent and that of T-DM1 is bivalent, the small difference in the required DAR could be attributed to stronger target binding of the T-DM1. Second, throughout the in vivo studies, we did not observe any serious adverse effects such as liver toxicity, loss of weight, or animal death (Figure S6, S7). Third, due to the mirror-image nature, L-form nucleic acids has low immunogenic potential and it cannot be recognized by immune receptors such as toll-like receptors. To the best of our knowledge, there was no immune response detected for the three L-form nucleic acid drug candidates in clinical trials (spiegelmers NOX-H94, NOX-E36 and NOX-A12).[24,33] Finally, the assembled L–DNA tetramer with a MW of ≈40 kDa showed surprisingly speedy renal clearance as significant amount of intact tetrameric assembly was detected in urine. With Cy5.5 labeled L–DNA, we found that ≈80 % of the L–DNA tetramer was cleared within 24 h and ≈100 % within 48 h (Figure S11). Among six tissues (brain, heart, liver, stomach, kidney, bladder) collected at different time points, kidney and liver showed the greatest uptake of L–DNAs as indicated by fluorescence intensity (Figure S11a). The fluorescence in kidney and liver, however, reduced sharply over time and reached the level of PBS control after 168 h (Figure S11b). Collectively, our data suggest that MADCs prepared via self-assembly of L–DNA linkers have the preclinical properties for advancing to clinical studies.

Acknowledgements

This work was supported by research funds from the Assembly Medicine, LLC.

Conflict of Interest

The authors declare no conflict of interest.

Data Availability Statement

The data that support the findings of this study are available in the supplementary material of this article.

Keywords: Antibody-Drug Conjugate Library · Modular Antibody-Drug Conjugate · Multispecificity · Nucleic Acid Linker · Self-Assembly

[1] a) A. Mullard, *Nat. Rev. Drug Discovery* **2013**, *12*, 329–332; b) J. Z. Drago, S. Modi, S. Chandarlapaty, *Nat. Rev. Clin. Oncol.* **2021**, *18*, 327–344.

[2] a) F. L. Moolten, S. R. Cooperband, *Science* **1970**, *169*, 68–70; b) G. F. Rowland, G. J. O'Neill, D. A. Davies, *Nature* **1975**, *255*, 487–488; c) K. Strebhardt, A. Ullrich, *Nat. Rev. Cancer* **2008**, *8*, 473–480.

[3] J. M. Lambert, A. Berkenblit, *Annu. Rev. Med.* **2018**, *69*, 191–207.

[4] L. Wang, G. Amphlett, W. A. Blattler, J. M. Lambert, W. Zhang, *Protein Sci.* **2005**, *14*, 2436–2446.

[5] J. Lu, F. Jiang, A. Lu, G. Zhang, *Int. J. Mol. Sci.* **2016**, *17*, 561.

[6] S. Garcia-Alonso, A. Ocana, A. Pandiella, *Cancer Res.* **2018**, *78*, 2159–2165.

[7] S. J. Walsh, J. D. Bargh, F. M. Dannheim, A. R. Hanby, H. Seki, A. J. Counsell, X. Ou, E. Fowler, N. Ashman, Y. Takada, A. Isidro-Llobet, J. S. Parker, J. S. Carroll, D. R. Spring, *Chem. Soc. Rev.* **2021**, *50*, 1305–1353.

[8] a) J. R. Junutula, H. Raab, S. Clark, S. Bhakta, D. D. Leipold, S. Weir, Y. Chen, M. Simpson, S. P. Tsai, M. S. Dennis, Y. Lu, Y. G. Meng, C. Ng, J. Yang, C. C. Lee, E. Duenas, J. Gorrell, V. Katta, A. Kim, K. McDorman, K. Flagella, R. Venook, S. Ross, S. D. Spencer, W. Lee Wong, H. B. Lowman, R. Vandlen, M. X. Sliwkowski, R. H. Scheller, P. Polakis, W. Mallet, *Nat. Biotechnol.* **2008**, *26*, 925–932; b) B. Q. Shen, K. Xu, L. Liu, H. Raab, S. Bhakta, M. Kenrick, K. L. Parsons-Reponte, J. Tien, S. F. Yu, E. Mai, D. Li, J. Tibbitts, J. Baudys, O. M. Saad, S. J. Scales, P. J. McDonald, P. E. Hass, C. Eigenbrot, T. Nguyen, W. A. Solis, R. N. Fuji, K. M. Flagella, D. Patel, S. D. Spencer, L. A. Khawli, A. Ebens, W. L. Wong, R. Vandlen, S. Kaur, M. X. Sliwkowski, R. H. Scheller, P. Polakis, J. R. Junutula, *Nat. Biotechnol.* **2012**, *30*, 184–189.

[9] H. Schneider, L. Deweid, O. Avrutina, H. Kolmar, *Anal. Biochem.* **2020**, *595*, 113615.

[10] S. O. Doronina, B. E. Toki, M. Y. Torgov, B. A. Mendelsohn, C. G. Cerveny, D. F. Chace, R. L. DeBlanc, R. P. Gearing, T. D. Bovee, C. B. Siegall, J. A. Francisco, A. F. Wahl, D. L. Meyer, P. D. Senter, *Nat. Biotechnol.* **2003**, *21*, 778–784.

[11] G. Leriche, M. Nothisen, N. Baumlin, C. D. Muller, D. Bagnard, J. S. Remy, S. A. Jacques, A. Wagner, *Bioconjugate Chem.* **2015**, *26*, 1461–1465.

[12] a) R. R. Nani, A. P. Gorka, T. Nagaya, T. Yamamoto, J. Ivanic, H. Kobayashi, M. J. Schnermann, *ACS Cent. Sci.* **2017**, *3*, 329–337; b) A. Dal Corso, L. Pignataro, L. Belvisi, C. Gennari, *Chemistry* **2019**, *25*, 14740–14757.

[13] C. M. McKertish, V. Kayser, *Biomedicine* **2021**, *9*, 872.

[14] A. Beck, L. Goetsch, C. Dumontet, N. Corvaia, *Nat. Rev. Drug Discovery* **2017**, *16*, 315–337.

[15] J. C. Thery, J. P. Spano, D. Azria, E. Raymond, F. Penault L-lorca, *Eur. J. Cancer* **2014**, *50*, 892–901.

[16] a) P. Nagy, E. Friedlander, M. Tanner, A. I. Kapanen, K. L. Carraway, J. Isola, T. M. Jovin, *Cancer Res.* **2005**, *65*, 473–482; b) M. Scaltriti, F. Rojo, A. Ocana, J. Anido, M. Guzman, J. Cortes, S. Di Cosimo, X. Matias-Guiu, S. Ramon y Cajal, J. Arribas, J. Baselga, *J. Natl. Cancer Inst.* **2007**, *99*, 628–638.

[17] D. M. Collins, B. Bossenmaier, G. Kollmorgen, G. Niederfellner, *Cancers* **2019**, *11*, 394.

[18] G. Li, J. Guo, B. Q. Shen, D. B. Yadav, M. X. Sliwkowski, L. M. Crocker, J. A. Lacap, G. D. L. Phillips, *Mol. Cancer Ther.* **2018**, *17*, 1441–1453.

[19] C. M. Yamazaki, A. Yamaguchi, Y. Anami, W. Xiong, Y. Otani, J. Lee, N. T. Ueno, N. Zhang, Z. An, K. Tsuchikama, *Nat. Commun.* **2021**, *12*, 3528.

[20] J. Y. Li, S. R. Perry, V. Muniz-Medina, X. Wang, L. K. Wetzel, M. C. Rebelatto, M. J. Hinrichs, B. Z. Bezabeh, R. L. Fleming, N. Dimasi, H. Feng, D. Toader, A. Q. Yuan, L. Xu, J. Lin, C. Gao, H. Wu, R. Dixit, J. K. Osbourn, S. R. Coats, *Cancer Cell* **2016**, *29*, 117–129.

[21] a) M. R. Levengood, X. Zhang, J. H. Hunter, K. K. Emmerton, J. B. Miyamoto, T. S. Lewis, P. D. Senter, *Angew. Chem. Int. Ed.* **2017**, *56*, 733–737; b) A. Kumar, K. Kinneer, L. Masterson, E. Ezeadi, P. Howard, H. Wu, C. Gao, N. Dimasi, *Bioorg. Med. Chem. Lett.* **2018**, *28*, 3617–3621; c) N. Nilchan, X. Li, L. Pedzisa, A. R. Nanna, W. R. Roush, C. Rader, *Antibody Ther.* **2019**, *2*, 71–78.

[22] a) S. A. Kazane, J. Y. Axup, C. H. Kim, M. Ciobanu, E. D. Wold, S. Barluenga, B. A. Hutchins, P. G. Schultz, N. Winssinger, V. V. Smider, *J. Am. Chem. Soc.* **2013**, *135*, 340–346; b) L. Pan, C. Cao, C. Run, L. Zhou, J. J. Chou, *Adv. Sci.* **2020**, *7*, 1900973; c) A. Märcher, M. A. D. Nijenhuis, K. V. Gothelf, *Angew. Chem. Int. Ed.* **2021**, *60*, 21691–21696; d) I. Dovgan, A. Ehkirch, V. Lehot, I. Kuhn, O. Koniev, S. Kolodych, A. Hentz, M. Ripoll, S. Ursuegui, M. Nothisen, S. Cianferani, A. Wagner, *Sci. Rep.* **2020**, *10*, 7691.

[23] a) K. P. Williams, X. H. Liu, T. N. Schumacher, H. Y. Lin, D. A. Ausiello, P. S. Kim, D. P. Bartel, *Proc. Natl. Acad. Sci. USA* **1997**, *94*, 11285–11290; b) M. J. Damha, P. A. Giannaris, P. Marfey, *Biochemistry* **1994**, *33*, 7877–7885.

[24] M. Boyce, S. Warrington, B. Cortezi, S. Zollner, S. Vauleon, D. W. Swinkels, L. Summo, F. Schwoebel, K. Riecke, *Br. J. Pharmacol.* **2016**, *173*, 1580–1588.

[25] R. P. Lyon, T. D. Bovee, S. O. Doronina, P. J. Burke, J. H. Hunter, H. D. Neff-LaFord, M. Jonas, M. E. Anderson, J. R. Setter, P. D. Senter, *Nat. Biotechnol.* **2015**, *33*, 733–735.

[26] a) R. L. Chang, I. F. Ueki, J. L. Troy, W. M. Deen, C. R. Robertson, B. M. Brenner, *Biophys. J.* **1975**, *15*, 887–906; b) C. Kurts, U. Panzer, H. J. Anders, A. J. Rees, *Nat. Rev. Immunol.* **2013**, *13*, 738–753.

[27] M. Pruszynski, E. Koumarianou, G. Vaidyanathan, H. Revets, N. Devoogdt, T. Lahoutte, M. R. Zalutsky, *Nucl. Med. Biol.* **2013**, *40*, 52–59.

[28] B. Els Anna Alice Beirnaert, M. Hilde Adi Pierrette Meise, M. Hendricus Renerus Jacobus Mattheus Hoogenboon, H. Heidi Maria Florence Jonckheere, S. Torsten Dreier, US Patent 2010113339, **2010**.

[29] M. Hilde Adi Pierrette Revets, W. Carlo Boutton, M. Hendricus Renerus Jacobus Mattheus Hoogenboom, US Patent 8975382-B2, **2015**.

[30] a) G. D. Lewis Phillips, G. Li, D. L. Dugger, L. M. Crocker, K. L. Parsons, E. Mai, W. A. Blattler, J. M. Lambert, R. V. Chari, R. J. Lutz, W. L. Wong, F. S. Jacobson, H. Koeppen, R. H. Schwall, S. R. Kenkare-Mitra, S. D. Spencer, M. X. Sliwkowski, *Cancer Res.* **2008**, *68*, 9280–9290; b) J. M. Lambert, R. V. Chari, *J. Med. Chem.* **2014**, *57*, 6949–6964.

[31] P. Carter, L. Presta, C. M. Gorman, J. B. Ridgway, D. Henner, W. L. Wong, A. M. Rowland, C. Kotts, M. E. Carver, H. M. Shepard, *Proc. Natl. Acad. Sci. USA* **1992**, *89*, 4285–4289.

[32] a) A. Q. Dean, S. Luo, J. D. Twomey, B. Zhang, *mAbs* **2021**, *13*, 1951427; b) V. Kostova, P. Desos, J. B. Starck, A. Kotschy, *Pharmaceuticals (Basel)* **2021**, *14*, 442.

[33] a) A. Vater, S. Klussmann, *Drug Discovery Today* **2015**, *20*, 147–155; b) A. Vater, J. Sahlmann, N. Kroger, S. Zollner, M. Lioznov, C. Maasch, K. Buchner, D. Vossmeyer, F. Schwoebel, W. G. Purschke, S. Vonhoff, A. Kruschinski, K. Hubel, M. Humphrey, S. Klussmann, F. Fliegert, *Clin. Pharmacol. Ther.* **2013**, *94*, 150–157.

Manuscript received: February 23, 2023
Accepted manuscript online: March 24, 2023
Version of record online: ■■, ■■

Forschungsartikel

Antibody-Drug Conjugates

L. Zhou, F. Yang,* Z. Bai, X. Zhou, Z. Zhang, Z. Li, J. Gong, J. Yu, L. Pan, C. Cao,* J. J. Chou **e202302805**

Self-Assembled L–DNA Linkers for Rapid Construction of Multi-Specific Antibody-Drug Conjugates Library

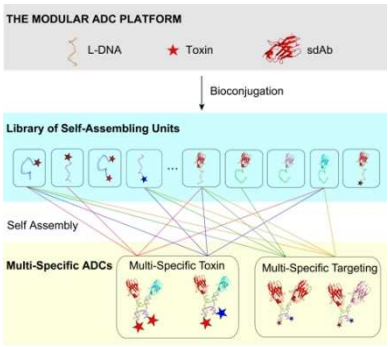

A modular platform for rapid construction of multi-specific Antibody-Drug Conjugates (ADCs). The MADC platform offers the combinatorial flexibility to screen for optimal target and payload combinations, while having the potential of becoming viable therapeutic agents themselves.

Angewandte Chemie
Eine Zeitschrift der Gesellschaft Deutscher Chemiker

Supporting Information

Self-Assembled L–DNA Linkers for Rapid Construction of Multi-Specific Antibody-Drug Conjugates Library

L. Zhou, F. Yang, Z. Bai, X. Zhou, Z. Zhang, Z. Li, J. Gong, J. Yu, L. Pan, C. Cao*, J. J. Chou*

Supporting Information

Self-Assembled L-DNA Linkers for Rapid Construction of Multi-Specific Antibody-Drug Conjugates Library

Liujuan Zhou, Fan Yang*, Zhaoshuai Bai, Xiaohui Zhou, Zhihai Zhang, Zhihang Li, Junyuan Gong, Junqi Yu, Liqiang Pan, Chan Cao*, James J. Chou

Abstract: One of the key challenges of improving ADC clinical outcomes of antibody drug conjugates (ADCs) is overcoming cancer resistance to the antibody and/or drug components of ADCs, and hence the need for ADC platforms with high combinatory flexibility. Here, we introduce the use of self-assembled left-handed DNA (L-DNA) oligonucleotides to link combinatory single-domain antibodies and toxin payloads for tunable and adaptive delivery of ADCs. We demonstrate that the method allows convenient construction of a library of ADCs with multi-specific targeting, multi-specific payloads, and exact drug-antibody ratio. The newly constructed ADCs with L-DNA scaffold showed favorable properties of *in vitro* cell cytotoxicity and *in vivo* suppression and eradication of solid tumors. Collectively, our data suggest that the L-DNA based modular ADC (MADC) platform is a viable option for generating therapeutic ADCs and for potentially expanding ADC therapeutic window via multi-specificity.

DOI: XXXX

SUPPORTING INFORMATION

Table of Contents

SUPPORTING INFORMATION

Materials

Key reagents

Trastuzumab-DM1 (HY-P9932), SPDB-DM4 (HY-12460), MC-VC-PAB-duocarmycin chloride (HY-128904), MC-VC-PAB-MMAE (HY-15575), MC-VC-PAB-MMAF (HY-112786), Deruxtecan (HY-13631E), and MC-VC-PAB-SN38 (HY-131057) were purchased from MedChemExpress. Osu-Glu-vc-PAB-MMAE (R-BR-106) was purchased from RuixiBio. Cyanine5.5 NHS ester (27020) were purchased from Lumiprobe. pHrodo™ Red, SE (P36600) was purchased from Thermo Fisher Scientific. The 5' and 3' modified L-DNA fragments were synthesized and purified by Hongene Biotech.

Cell lines and culture

SK-BR-3, HCC1954 cell lines were grown in RPMI1640 medium (Gibco, 21870076) supplemented with 10% FBS (Gibco, 10099141C). JIMT-1 cell lines were grown in DMEM medium (Gibco, 11965092) supplemented with 10% FBS. SK-OV-3 cell line was grown in McCoy's 5A medium (Gibco, 16600082) supplemented with 10% FBS. All cell lines were cultured at 37˚C humidified incubator with 5% CO_2 and 95% air. Growth medium was renewed every 2 or 3 days and cells were subcultured once and about 80% confluence has been reached.

Methods

Metropolis Monti Carlo simulation with Simulated Annealing (MMCSSA)

For tetrameric self-assembly, we adopted the classic Holliday junction structure but enforced top-down and left-right mirror symmetry to simplify sequence design (Fig. 2a). Iterative optimization of the DNA sequences involved the following steps (Fig. 2b):

(1) Sequence initialization. Each of the 4 DNA chains in Fig. 2a has the format

$$S_1 = (5')X_1 - R_1 - L - R_2(3'),$$

where R_1 and R_2 are the two variable segments for inter-chain pairing, X1 is the 5' handle (set to 'A' in this study), and L is a constant linker between R1 and R2 (also set to 'A' in this study). Both R1 and R2 are 16 bases long. Hence each of the S1-S4 DNA chains is 34 bases long. The R1 and R2 sequences of the first DNA chain (S1) were randomly generated to satisfy the following criteria.

(a) In order to ensure sufficient stability of the wanted double-stranded pairing, the free energy (ΔG) of R1 complementary pairing and R2 complementary pairing are set to be less than -27 kcal/mol, which yields a melting temperature (T_m) of ~52 ºC. ΔG is calculated as the summation of ΔG of base pairing according to the nearest-neighbor rule, as previously described[1]. For example, the equation for calculating the ΔG of double-strand formation for a DNA sequence $b_1 b_2 \ldots b_n$ is

$$\Delta G = \sum_{i=1}^{n-1} \Delta G(b_i b_{i+1}),$$

where $\Delta G(b_i b_{i+1})$ is the nearest-neighbor free energy for Watson-Crick pairing at 50 mM Na^+. The calculation method we used in this paper is consistent with that given on IDT website (www.idtdna.com), with an average discrepancy less than 0.05 kcal/mol for 34 bps.

(b) Likewise, to minimize the unwanted homotypic interaction of S1, the ΔG of S1 homodimerization is set to be greater than -7 kcal/mol.

(c) In order to maintain sufficient base diversity of the DNA sequence, the fraction of each base type (A, T, C, or G) must be greater than or equal to 15% and the difference between the largest and smallest fractions must not be more than 35%.

After the initialization of S1 sequence, the sequences of S2, S3, and S4 are generated by applying the mirror symmetry shown in Fig. 2a.

(2) Calculating the base-pairing energy matrices. The goal of the optimization is to maximize the intended strand pairing while minimizing the off-target pairing. Thus, an interaction energy matrix **M**(ΔG) is constructed containing ΔG values of all possible double-stranded pairing, specific (intended) and non-specific (unwanted) between the variable segments (*R*). In the case of tetramer, each of the 4 chains has 2 variable segments to pair with different chains (hence 8 segments). The matrix is 8 x 8 (**M**$(\Delta G)_{8x8}$) in which each element ΔG_{ij} is the free energy of base pairing between segments *i* and *j*, *i, j* = 1-8. Of note, the matrix **M**$(\Delta G)_{ij}$ contains ΔG values from both specific (ΔG_{ij}^{S}) and non-specific (ΔG_{ij}^{NS}) segment pairings.

The initial sequences are evaluated for the total free energy of unwanted pairing, defined as

$$E^{NS} = \sum_{i=1}^{n} \sum_{j=1}^{n} \Delta G_{ij}^{NS}, \; n = 8,$$

where ΔG_{ij}^{NS}=0 for specific (intended) base pairing between R_i and R_j. That is, E^{NS} is defined as the sum of all ΔG values of base pairings between R_i and R_j that are not supposed to pair, including those between the same segments.

(3) Locating the worst off-target base pairing region to repair. During the calculation of ΔG_{ij}^{NS} between R_i and R_j that are not supposed to pair, R_j is slid against R_i, one base at a time, from R_i 5' end to 3' end. ΔG is calculated at each position. The pairing position with the lowest ΔG value is recorded as the non-specific pairing position, and $\Delta G_{ij}^{NS}=\Delta G$. Hence, to locate the most pronounced off-target base pairing region, the lowest ΔG_{ij}^{NS} in $\mathbf{M}(\Delta G)_{8x8}$ is first identified and then the corresponding pairing position of R_i and R_j are retrieved. The bases involved in non-specific pairing within the R_i and R_j were designated for repair.

(4) Random mutagenesis of the repair region. For the above identified region of unwanted base pairing, the bases are randomly mutated. Specifically, for the region encompassing the most unwanted base pairings (bases B_k – B_l of R_i, *k* and *l* denoting the beginning and the end of the region), all bases are randomly replaced with A, G, C, or T.

(5) Updating the sequences based on the mutations. After the base mutations are performed, the sequences of S1-S4 are updated to satisfy the mirror symmetry shown in Fig. 2a. In addition, the new sequences must meet the following criteria. (a) Free energy of the specific pairing segments (ΔG_{ij}^{S}) is less than -27.4 kcal/mol, which corresponds to a T_m of ~52 ºC. (b) CG content kept between 40% and 60%. If any of the above criteria is not met, steps 4-5 are repeated until the criteria are satisfied.

(6) Metropolis criterion for acceptance of mutagenesis. Next, the total free energy of unwanted pairing of the new sequences ($E^{NS\prime}$) is calculated, and the energy difference after the mutation is calculated as $\Delta E = E^{NS} - E^{NS\prime}$. The ΔE is then used for determining whether to accept the mutation according to the Metropolis criterion. Define the probability function $p = exp(-\Delta E/T)$ and generate a random number *r* between 0 and 1. *T* is an empirical temperature used for simulated annealing. If p > *r*, the mutation is accepted ($E^{NS} = E^{NS\prime}$). Otherwise, the mutation is rejected. Repeat steps 3-6.

(7) Simulated annealing. Steps 4-7 are repeated for 10 times at a fixed *T* before *T* is decreased by a factor λ ($T = T \times \lambda$). In our study, we experimented with a range of values for initial *T* (T_i), final *T* (T_f), and λ. The values that yielded the best convergence are $T_i = 50$℃, $T_f = 0.12$℃, $\lambda = 0.985$. When E^{NS} is no longer decreasing for 2000 iterations, or when *T* is less than T_f, the optimization routine stops.

The above steps 1-7 were repeated for 60 times and 60 sequence solutions were obtained. These sequences were than screened against the human genome database to find a solution which has the least homology or pairing potential with any region of the human DNA. About 4 solutions were identified that performed very similarly in both off-target pairing energy, intended pairing energy, and sequence overlap with human DNA. A representative solution is shown in Fig. 2c. The calculated T_m of the four arms of the assembled tetramer (S1-S4, S1-S2, S2-S3, S3-S4) are 50 °C, 49.6 °C, 49.6°C, and 49.6 °C, respectively. Furthermore, non-specific basepairing is very minimal among the S1-S4 sequences (see Fig. S12) as independently validated by the IDT oligo analyzer (https://sg.idtdna.com/calc/analyzer).

sdAb expression and purification

The genes encoding the sdAb targeting HER2 extracellular domain II named 47D05 (L108Q)[2], the sdAb targeting HER2 extracellular domain IV named 5F07(Q108L)[2] and the sdAb targeting HSA named Alb1[3] were codon optimized and synthesized for *pichia pastoris* expression. In addition, each of the genes contains a polyhistidine-tag at the N-terminus and a "GSC" sequence at the C-terminus and was subcloned into the pPICZα A vector (Invitrogen). The expression plasmids were linearized with endonuclease BstX I (BioLabs, R0113S)/Pme I (BioLabs, R0560S) for overnight at 4˚C, ethanol precipitated and inserted by electroporation into the *pichia pastoris* X33 strain (Invitrogen, 2253254). The transformants carrying integrated expression cassettes with zeocin resistance were selected on YPD-agar plates with 200, 400, 600, 800 μg/mL zeocin (Invitrogen, R25001) and verified by PCR analysis to make sure the recombinant plasmids were correctly transformed and integrated into the genome of *pichia pastoris* X33. Several transformants were used to screen for high-expression clones by performing 4-12% SDS-PAGE of culture supernatant after methanol induction. Clones expressing the highest amount of sdAb were chosen for further sdAb production.

The selected clones expressing recombinant anti-HER2 sdAbs or anti-HSA sdAb were inoculated in 5 mL BMGY (Sangon, B540130) in a sterile 50 mL Falcon tube and incubated overnight at 30˚C with constant shaking at 250 rpm. The cells were centrifuged (5 min, 3000 x g) and the pellet was resuspended in 100 mL fresh BMGY medium in a 1 L baffled flask and incubated at 30 ˚C with constant shaking at 250 rpm for 48~72h. Cells were harvested and then induced for secreted expression in 50 mL BMMY (Sangon, B540131) at 30˚C with constant shaking at 250 rpm for 72~84h, during which the culture were supplemented with 100% methanol (Adamas-beta) to a final concentration of 1%(v/v) every 24h. Finally, culture supernatant containing sdAb were separated from cells by centrifuging at 3000 x g for 10 min after induction. The sdAbs were purified by Ni-NTA column (Cytiva) and stored at -80 ˚C.

SUPPORTING INFORMATION

sdAb-(L-DNA) conjugation

The L-DNA with a 5'-NH_2 group was first conjugated with $SM(PEG)_2$ (Thermo, 22102) as described previously[4]. Briefly, 5'-NH_2 modified L-DNA was mixed with $SM(PEG)_2$ in a molar ratio of 1:50 in PBS buffer (50 mM NaH_2PO_4, 150 mM NaCl, pH 7.4) and incubated at 25˚C for 2h. Then $SM(PEG)_2$-L-DNA was purified by ethanol precipitation and solubilized in ultrapure water. Subsequently, the sdAb was dialyzed against a Tris buffer (20 mM Tris, 150 mM NaCl, pH 7.4) containing 10-fold molar excess of TCEP (Thermo, PG82089) to keep the free thiol at the sdAb C-terminus reduced. The sdAb solution was mixed with $SM(PEG)_2$-L-DNA at a molar ratio of sdAb : $SM(PEG)_2$-L-DNA of 1:1–1:2 at room temperature for 2h. The conjugation efficiency was examined using 4-12% SDS-PAGE (GeneScript, M00654). The reaction mixture was then loaded to a Ni-NTA column to remove unconjugated $SM(PEG)_2$-L-DNA. The eluted fraction containing unconjugated sdAb and sdAb-L-DNA was loaded to a Q column (Cytiva, HiTrap Q HP) equilibrated with Buffer A (20 mM Tris-HCl, 15 mM NaCl, pH 8.5) and eluted with a 30 CV linear gradient of 0-100% Buffer B (20 mM Tris-HCl, 1 M NaCl, pH 8.5) at a flow rate of 1 mL/min. The elution fractions containing sdAb-L-DNA were collected, followed by buffer exchange to PBS (BasalMedia, B320KJ). The purity of sdAb-L-DNA was examined using negative ion mode LC-MS (Thermo, LTQ).

Payload-(L-DNA) conjugation

For conjugating toxin to L-DNA with NH_2 moiety, the NH_2 modified L-DNA was dissolved in PBS (10 mM Na_2HPO_4, 1.8 mM KH_2PO_4, 2.7 mM KCl, 137 mM NaCl, pH 7.4) at 1 mM concentration and then mixed with 50-70 equivalents of payload (Osu-Glu-vc-PAB-MMAE or SPDB-DM4) that was pre-dissolved in PBS/DMA (40/60 wt%) at 20 mM stock concentration. The reaction mixture was incubated at 45˚C for 20-24h. The yields of conjugation reactions were monitored using 4% agarose gel electrophoresis. After the reaction was completed, the excess payloads were removed by ethanol precipitation. Finally, the precipitated payload-L-DNA conjugates were solubilized in PBS (BasalMedia, B320KJ) and the purity was examined using negative ion mode LC-MS (Thermo, LTQ).

For conjugating toxin to L-DNA with SH moiety, the thiol modified L-DNA was dissolved in Tris buffer (20 mM Tris, 150 mM NaCl, pH 7.5) containing 10-fold molar excess of TCEP, which was used to reduce the free thiol on the 5' or 3' end of the L-DNA. The reduced L-DNA was ethanol precipitated and solubilized again at 1 mM stock concentration in the same Tris buffer containing 1 mM TCEP. The L-DNA solution was then mixed with molar 20 equivalents of maleimide-containing payload (MC-VC-PAB-duocarmycin chloride, MC-VC-MMAE, MC-VC-MMAF, Deruxtecan, or MC-VC-PAB-SN38) that was dissolved in DMSO at 20 mM stock solution. The pH of the reaction mixture was adjusted to within the range of 6.5–7.5 with few drops of 1M stock of Tris buffer (pH 7.5). The reaction mixture was incubated at room temperature for 4–8h, and the yields of conjugation reactions were monitored with 4% agarose gel electrophoresis. After the reaction was completed, the excess payloads were removed by ethanol precipitation. The precipitated payload-L-DNA conjugates were solubilized in PBS and the purity was examined using negative ion mode LC-MS (Thermo, LTQ).

MADC assembly

All MADCs used in this study comprise 4 assembly units. Taking anti-HER2 MADC drug D (Table S2) as an example, it is composed of MMAE-S1, MMAE-S2, HER2-S3, and HER2-S4 (MADC Module No. 1, 2, 11 and 14 in Table S1). Thus, anti-HER2 MADC drug D was prepared by mixing equal moles of the 4 assembly units. Other MADCs were prepared in the same way by mixing equal moles of 4 designated assembly units.

BLI measurement of MADC affinity to target antigens

Binding affinity of anti-HER2 MADC drug A (Table S2) to HER2 and HSA protein was measured by bio-layer interferometry (BLI) using the Octet RED96e instrument (ForteBio). For binding to HER2, Fc-tagged HER2 (Acro biosystems, HE2-H5253) was immobilized onto AHC biosensor at a concentration of 10 µg/mL. Then, anti-HER2 MADC drug A in BLI buffer (1×PBS, pH 7.4, 0.02% Tween-20, 0.1% BSA) was loaded at decreasing concentrations of 100, 50, 25, 12.5, 6.25, and 3.125 nM. The association time was 90s, and the dissociation time was 180s. For binding to the human serum albumin (HSA), biotinylated HSA (Acro biosystems, HSA-H82E3) was immobilized onto SA biosensor at a concentration of 10 µg/mL. Then, anti-HER2 MADC drug A in BLI buffer (1×PBS, pH 7.4, 0.02% Tween-20, 0.1% BSA) was loaded at decreasing concentrations of 500, 250, 125, 62.5, 31.25, and 15.625 nM. The association time was 60s, and the dissociation time was 120 s. Data were analyzed using DataAnalysis 11.

pHrodo Conjugation

For labeling MADC drug A or B (Table S2) with pH-sensitive fluorescent probe, Succinimidyl (NHS) ester modified pHrodo™ red was conjugated with a 5'-NH_2 modified L-DNA, which was then assembled with other 3 assembly units to form the pHrodo labeled MADC complex. NHS ester modified pHrodo was first dissolved in DMSO at 10 mM concentration and then mixed with the 5'-NH_2 modified L-DNA in a molar ratio of 20:1 in PBS buffer (50 mM NaH_2PO_4, 150 mM NaCl, pH 7.4), incubated at 25˚C for 2h. After conjugation, pHrodo-L-DNA was purified by ethanol precipitation and assembled with other assembly units to form a MADC complex, designated A-pHrodo or B-pHrodo.

SUPPORTING INFORMATION

For labeling the trastuzumab antibody with pHrodo, the NHS ester modified pHrodo was non-specifically conjugated with trastuzumab (MedChemExpress, HY-P9907) in a molar ratio of 20:1 in PBS buffer at 25˚C for 1h and purified by PD-10 (Cytiva, 17085101).

Internalization assay

For testing receptor-binding mediated internalization of MADCs, 20 nM of A-pHrodo, B-pHrodo or T-DM1-pHrodo were incubated with HCC1954 cells at 37˚C for 1, 3, 6, 22, 30 hours to allow internalization. Cell media were replaced with PBS and plates were read on SpectraMax i3x plate reader at Ex/Em of 560/585 nm. The net fluorescent signals (N_t) = F_t-F_0, F_t is the fluorescent signal of cells treated with drugs, F_0 is the average fluorescent signal of control cell wells treated with PBS. To compare internalization rate of drugs with different pHrodo labelling number, the net fluorescent signals were normalized using the equation: % net fluorescence = (N_t – N_{min})/(N_{max} – N_{min}) x 100, where N_t is the net fluorescent signal of cells treated with drugs for different incubation times, N_{min} is the minimum net fluorescent signal of cells (control wells), and N_{max} is the maximum net fluorescent signal of cells.

***In vitro* cell cytotoxicity assay**

Cells were seeded in a 96-well plate (Corning, 3603) at appropriate density (5000 – 8000 cells per well in 90 µL culture medium). After overnight incubation, cells were treated with 100, 20, 4, 0.8, 0.16, 0.032 and 0.0064 nM MADC drugs and incubated at 37˚C for 72h. 100 µL of the Cell Titer-Glo luminescent cell viability assay reagent (Promega, G7572) was added to each well and fluorescence was measured with a multimode microplate reader (Molecular Devices, SpectraMax i3x). The concentration values for 50% of maximal inhibition of cell proliferation (GI50) were calculated by the four-parameter logistic (4PL) model using GraphPad Prism 9. The mean percent growth inhibition was calculated as follows: %Growth Inhibition=(S_c-S_t)/(S_c-S_b)*100, S_c is the luminescent signal of negative control, S_t is the luminescent signal of samples at the end of the 72h drug incubation, S_b is the luminescent signal of samples at the beginning of the incubation.

***In vivo* tumor suppression efficacy study**

All animal tests involving the care and use of animals in this study will be reviewed and approved by the Institutional Animal Care and Use Committee (IACUC), the IACUC approved number is LDIACUC005. During the study, the care and use of animals will be conducted in accordance with the regulations of the Association for Assessment and Accreditation of Laboratory Animal Care (AAALAC). HCC1954 cells were subcutaneously (s.c.) injected as a Matrigel suspension into the right flanks of female nude BALB/c nude mice (6-8 weeks old). Animals were randomly assigned into 6 groups (6 mice per group) when the tumor volume reached 100–200 mm^3. MADCs with DAR = 0, 2, 4, 6 (24 nmol/kg), Trastuzumab-DM1 (24 nmol/kg; positive control), and PBS (pH 7.4; negative control) were injected intravenously (i.v.) on days 0, 3, 6, 9, 12, 15, 18. Tumor size was monitored 3 times per week using caliper measurement, and tumor volume was calculated using the formula: T_{vol} (mm^3) = 0.5 × longer diameter × (shorter diameter)^2. In addition, the body weights of the mice were measured 4 times weekly. Animals were euthanized at day 47 post first MADC injection and tumors were collected and weighed.

In vivo toxicity study

All animal tests involving the care and use of animals in this study will be reviewed and approved by the Institutional Animal Care and Use Committee (IACUC), the IACUC approved number is LDIACUC005. During the study, the care and use of animals will be conducted in accordance with the regulations of the Association for Assessment and Accreditation of Laboratory Animal Care (AAALAC). For toxicity study, 6-8 weeks old female Sprague-Dawley rats were randomly assigned to 2 groups (n = 3) and were treated with a single intravenous injection of Drug E (Table S2) at a dose of 0.5 mg/kg or 5 mg/kg. 200 µL blood samples were collected from each animal via the jugular vein predose on days 5 and 14 post-injection. The samples were left at room temperature for 30 min until the blood coagulated. Then serum was obtained by centrifuging at 6800 x g for 6 min at 4˚C and stored at -80˚C. Each animal was observed twice daily for mortality, abnormalities, and signs of distress. Body weights were measured twice per week. AST and ALT levels were examined using ELISA kits (Jianglaibio) and the absorbance at 450 nm was recorded using a multi-mode microplate reader (Molecular Devices, SpectraMax i3x). All assays were performed in duplicates.

Table S1. MADC Inventory

NO.	NAME	MADC Inventory Module
1	MMAE-S1	MMAE-5'-AAGCAGCCTCGTTGAATCGCCAAGACACCT
2	MMAE-S2	MMAE-5'-AAGGTGTCTTGGCGAAAGTTGCTCCGACGA
3	S3-MMAE	5'- ATCGTCGGAGCAACTAAGCGGTTCTGTGGA -3'-MMAE
4	MMAE-S1-MMAE	MMAE-5'-AAGCAGCCTCGTTGAATCGCCAAGACACCT-3'-MMAE
5	MMAE-S2-MMAE	MMAE-5'-AAGGTGTCTTGGCGAAAGTTGCTCCGACGA-3'-MMAE
6	DM4-S2	DM4-5'-AAGGTGTCTTGGCGAAAGTTGCTCCGACGA
7	MMAF-S2	MMAF-5'-AAGGTGTCTTGGCGAAAGTTGCTCCGACGA
8	duocarmycin-S2	duocarmycin-5'-AAGGTGTCTTGGCGAAAGTTGCTCCGACGA
9	Dxd-S4	Dxd-5'-ATCCACAGAACCGCTATCAACGAGGCTGCT
10	SN38-S4	SN38-5'-ATCCACAGAACCGCTATCAACGAGGCTGCT
11	anti-HER2^{IV}-S3	Anti-HER2 domain IV sdAb -5'-ATCGTCGGAGCAACTAAGCGGTTCTGTGGA
12	anti-HER2^{IV}-S4	Anti-HER2 domain IV sdAb -5'-ATCCACAGAACCGCTATCAACGAGGCTGCT
13	anti-HER2^{II}-S4	Anti-HER2 domain II sdAb -5'-ATCCACAGAACCGCTATCAACGAGGCTGCT
14	anti-HSA-S4	Anti-HSA sdAb -5'-ATCCACAGAACCGCTATCAACGAGG CTGCT
15	anti-HER2^{IV}-S3-MMAE	Anti-HER2 domain IV sdAb -5'-ATCGTCGGAGCAACTAAGCGGTTCTGTGGA -3'-MMAE
16	anti-HSA-S4-MMAE	Anti-HSA sdAb -5'-ATCCACAGAACCGCTATCAACGAGG CTGCT -3'-MMAE
17	S1	5'-AAGCAGCCTCGTTGAATCGCCAAGACACCT
18	S2	5'-AAGGTGTCTTGGCGAAAGTTGCTCCGACGA
19	S3	5'-ATCGTCGGAGCAACTAAGCGGTTCTGTGGA
20	S4	5'-ATCCACAGAACCGCTATCAACGAGGCTGCT
21	anti- HER2^{IV} -S1	Anti- HER2 domain IV sdAb -5'-AAGCAGCCTCGTTGAATCGCCAAGACACCT

Table S2. MADC Drugs

Name	Formats	MADC Inventory Module Assemble
Drug A	MADC-MMAE(1,1,2,2)-HER2(3)-HSA(4) (DAR=4)	MMAE-S1-MMAE (NO. 4) + MMAE-S2-MMAE (NO. 5) + anti-$HER2^{IV}$-S3 (NO. 11) + anti-HSA-S4 (NO. 14)
Drug B	MADC-MMAE(1,1,2,2)	MMAE-S1-MMAE (NO. 4) + MMAE-S2-MMAE (NO. 5) + S3 (NO. 19) + S4 (NO. 20)
Drug C	MADC-HER2(3)-HSA(4) (DAR=0)	S1 (NO. 17) + S2 (NO. 18) + anti-$HER2^{IV}$-S3 (NO. 11) + anti-HSA-S4 (NO. 14)
Drug D	MADC-MMAE(1,2)-HER2(3)-HSA(4) (DAR=2)	MMAE-S1 (NO. 1) + MMAE-S2 (NO. 2) + anti-$HER2^{IV}$-S3 (NO. 11) + anti-HSA-S4 (NO. 14)
Drug E	MADC-MMAE(1,1,2,2,3,4)-HER2(3)-HSA(4) (DAR=6)	MMAE-S1-MMAE (NO. 4) + MMAE-S2-MMAE (NO. 5) + anti-$HER2^{IV}$-S3-MMAE (NO. 15) + anti-HSA-S4-MMAE (NO. 16)
Drug F	MADC-MMAE(1,1,2,2)-HSA(4)	MMAE-S1-MMAE (NO. 4) + MMAE-S2-MMAE (NO. 5) + S3 (NO. 19) + anti-HSA-S4 (NO. 14)
Drug G	MADC-MMAE(2,2,3,4)-HER2(1,3)-HSA(4)	anti- $HER2^{IV}$-S1 (NO. 21)+ MMAE-S2-MMAE (NO. 5) + anti-$HER2^{IV}$-S3-MMAE (NO. 15) + anti-HSA-S4-MMAE (NO. 16)
Drug H	MADC-MMAE(1)-MMAF(2)-HER2(3)-HSA(4)	MMAE-S1 (NO. 1) + MMAF-S2 (NO. 7) + anti-$HER2^{IV}$-S3 (NO. 11) + anti-HSA-S4 (NO. 14)
Drug I	MADC-MMAE(1)-DM4(2)-HER2(3)-HSA(4)	MMAE-S1 (NO. 1) + DM4-S2 (NO. 6) + anti-$HER2^{IV}$-S3 (NO. 11) + anti-HSA-S4 (NO. 14)
Drug J	MADC-MMAE(1)-DuO(2)-HER2(3)-HSA(4)	MMAE-S1 (NO. 1) + DuO-S2 (NO. 8) + anti-$HER2^{IV}$-S3 (NO. 11) + anti-HSA-S4 (NO. 14)
Drug K	MADC-MMAE(1)-DuO(2)-$HER2^{IV}$(3)-$HER2^{IV}$(4)	MMAE-S1 (NO. 1) + DuO-S2 (NO. 8) + anti-$HER2^{IV}$-S3 (NO. 11) + anti-$HER2^{IV}$-S4 (NO. 12)
Drug L	MADC-MMAE(1)-DuO(2)-$HER2^{IV}$(3)-$HER2^{II}$(4)	MMAE-S1 (NO. 1) + DuO-S2 (NO. 8) + anti-$HER2^{IV}$-S3 (NO. 11) + anti-$HER2^{II}$-S4 (NO. 13)

Table S3. *In Vitro* Potency of Anti-HER2 MADCs with Different DAR in a Panel of Cancer Cell Lines

Cell Line	Cancer Type	Relative HER2 Density on Cell	In Vitro Cytotoxicity (Relative EC_{50} in nM)			
			MADC DAR=0	MADC DAR=2	MADC DAR=4	MADC DAR=6
SK-OV-3	ovarian	645000	inactive	4.305	2.139	0.484
HCC1954	breast	911000	inactive	0.596	0.251	0.176
SK-BR-3	breast	1132000	inactive	0.193	0.159	0.143

Table S4. Efficacy of MADCs of Different DAR with HCC-1954 CDX Model in BALB/c nude Mice

Group	N	Drug	DAR	Dose (mg/kg)	Route	Mean Tumor Volumn (mm^3)		TGI* (%)
						Mean±SEM / D0	Mean±SEM / D47	
1	6	Vehicle	--	--	i.v.	118.31±9.73	2703.38±924.69	--
2	6	C	0	1.8	i.v.	119.82±11.24	2095.31±502.96	23.58
3	6	D	2	1.8	i.v.	120.42±9.1	1667.47±409.01	40.15
4	6	A	4	1.8	i.v.	118.25±9.84	552.36±142.99	83.21
5	6	E	6	1.8	i.v.	118.73±10.02	33.39±5.24	103.30
6	6	T-DM1	3.5	3.6	i.v.	116.94±10.25	9.92±3.19	104.14

*Note: TGI（%）= $[1-(T_i-T_0)/(V_i-V_0)] \times 100$, in which T_i represents the mean tumor volume of a dosing group on day 47, T_0 is the mean tumor volume of a dosing group on day 0, V_i is the mean tumor volume of vehicle group on day 47, and V_0 is the mean tumor volume of vehicle group on day 0.

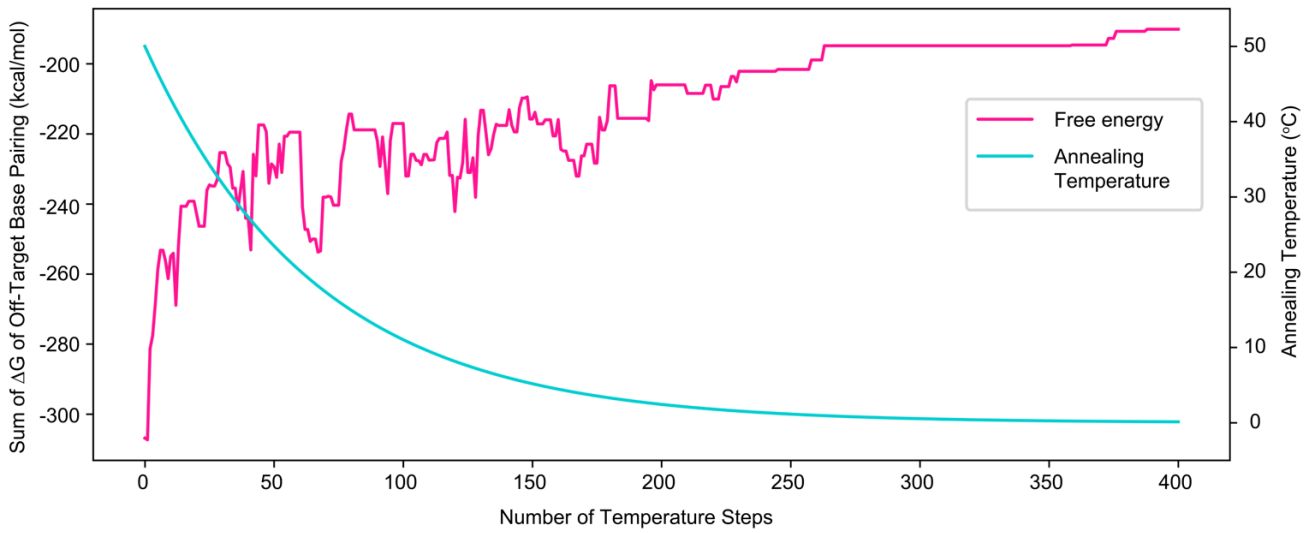

Figure S1. A typical simulated annealing trajectory for optimizing the tetramer sequences to achieve the maximum sum of ΔG of off-target base pairing (E^{NS}).

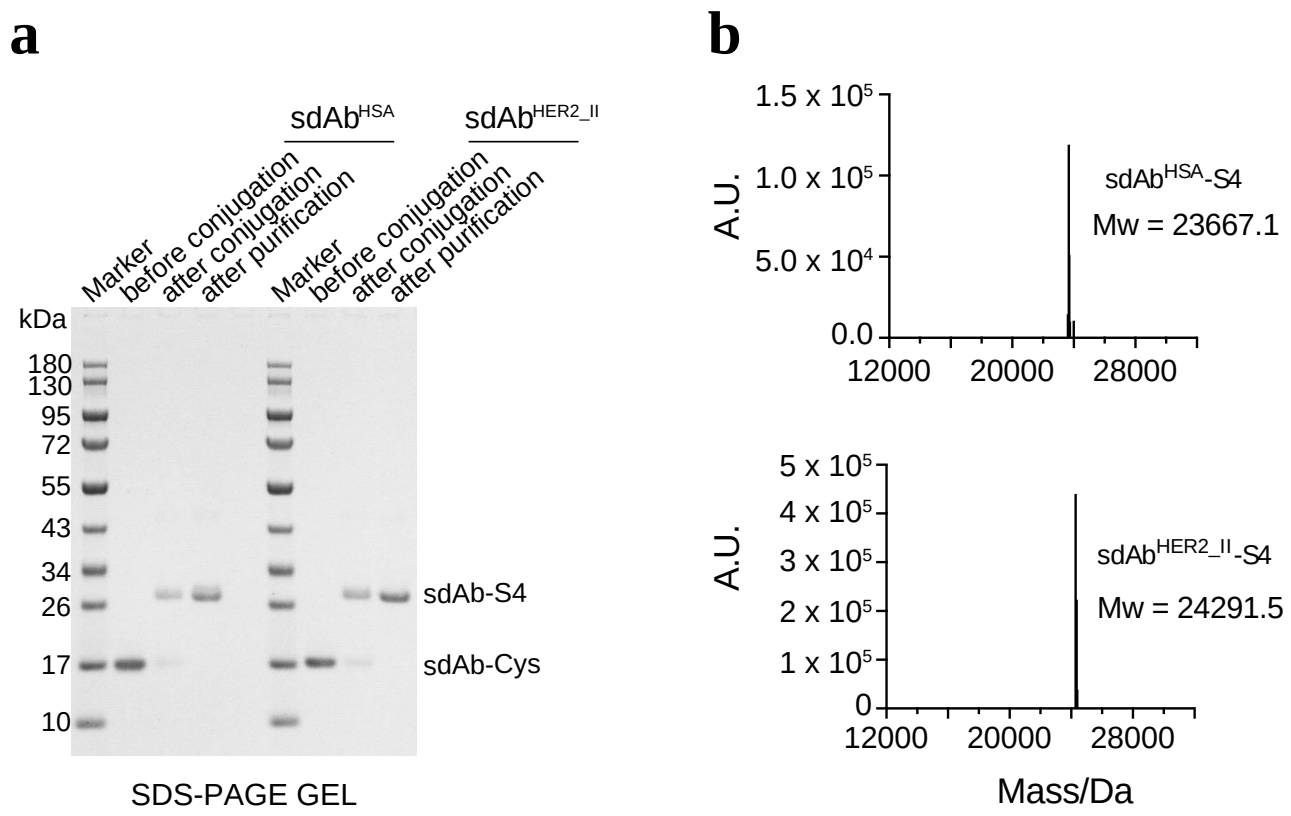

Figure S2. 5'-amino-L-DNA Conjugation with anti-HSA sdAb and anti-HER2^{II} sdAb. The conjugation efficiency was determined with gel electrophoresis (**a**) and ESI Mass Spectrum (**b**).

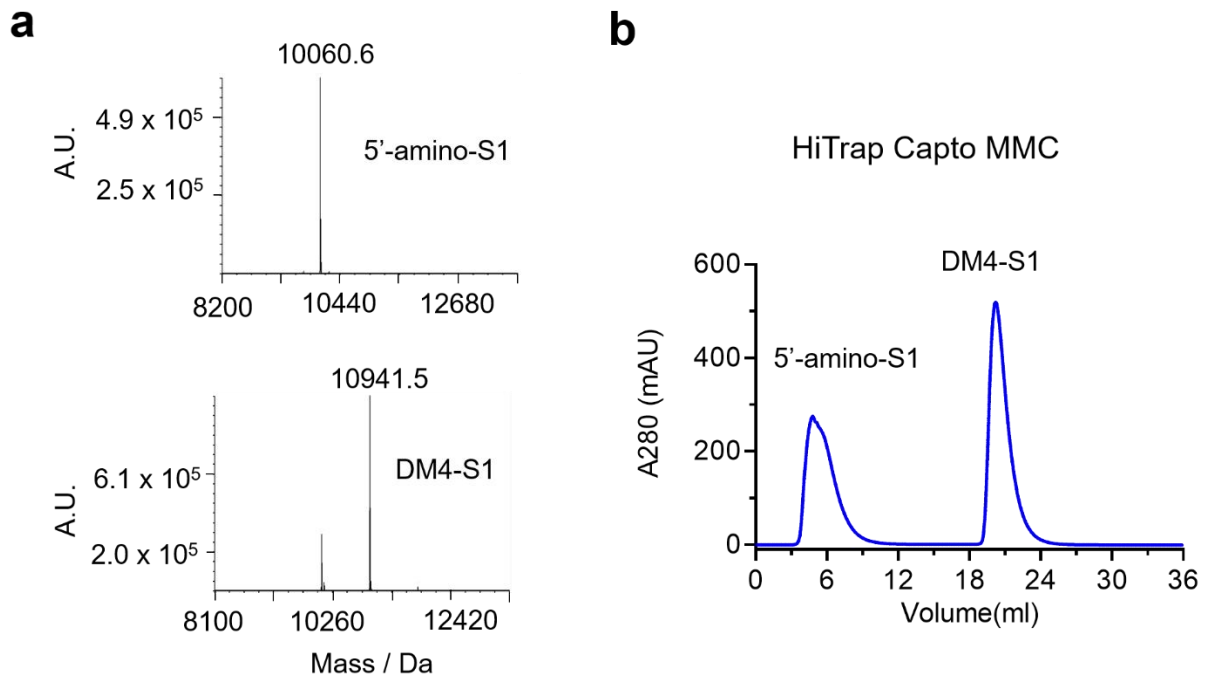

Figure S3. 5'-amino-L-DNA Conjugation with DM4. (**a**) Toxin DM4 was conjugated to 5'-end of L-DNA with SPDB linker. The conjugation efficiency was determined with ESI Mass Spectrum. (**b**) DM4-L-DNA can be purified with HiTrap Capto MMC column.

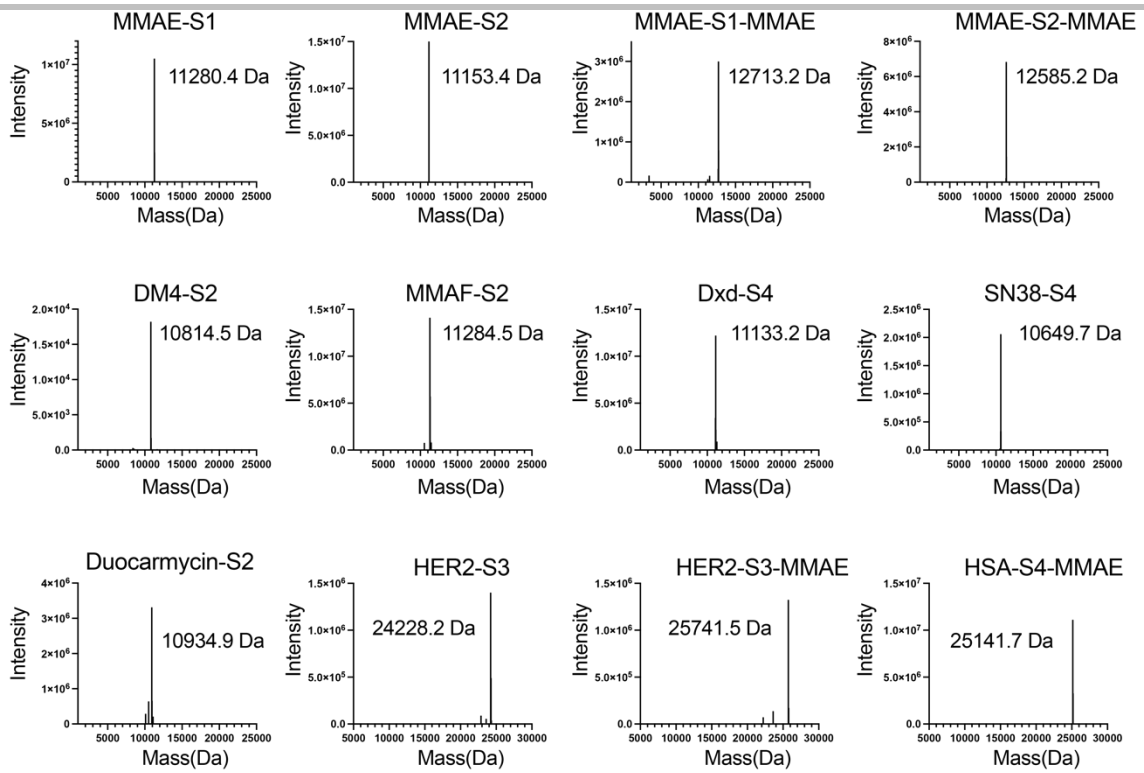

Figure S4. ESI mass spectroscopy analysis of sdAb-oligos, toxin-oligos and sdAb-oligo-toxin listed in Table S1.

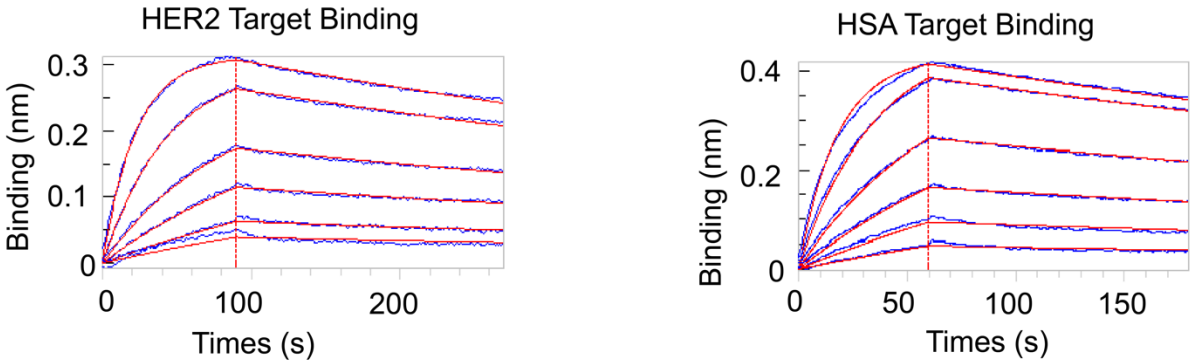

Drug	Antigen	K_{on} (1/Ms)	K_{off} (1/s)	K_D^{app} (nM)
anti-HER2 MADC	HER2	4.41E+05	1.33E-03	3.02
	HSA	1.08E+05	1.62E-03	15.03

Figure S5. Target binding affinities of the assembled anti-HER2 MADC Drug A. Plot of Bio-Layer Interferometry (BLI) signal as a function of time in which anti-HER2 MADC (Drug A) reacted with immobilized HER2 with concentration of 100, 50, 25, 12.5, 6.25, 3.13 nM (*left*), and immobilized HSA with concentration of 500, 250, 125, 62.5, 31.3,15.6 nM (*right*) (blue trace). The fitting curve using 'association then dissociation' model is shown in red, and vertical dashed line marks the beginning of the dissociation phase. The table summarizes kinetic parameters extracted from the above fitting curves, and the measured dissociation constants (K_D) were 3.02 nM for HER2 target, and 15.03 nM for HSA target.

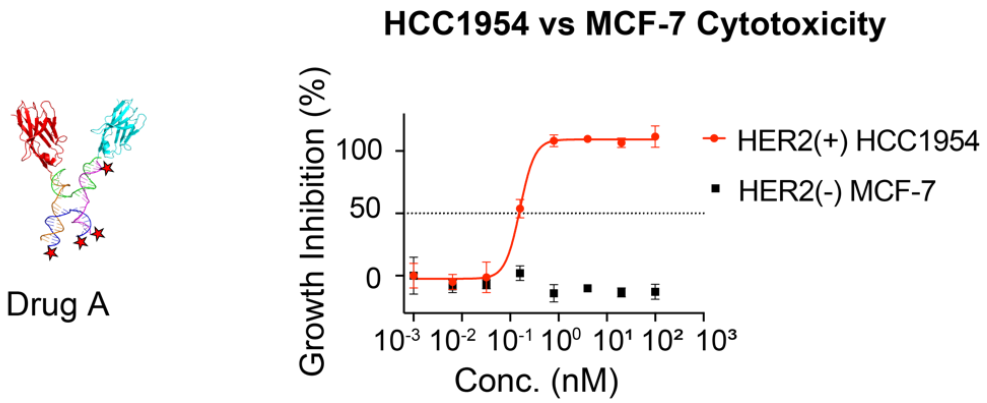

Figure S6. Effect of treating $HER2^+$ HCC1954 cells and $HER2^-$ MCF-7 cells with anti-HER2 MADC drug A at various concentration. Cell viability was measured by Cell Titer-Glo luminescent cell viability assay after 72h of incubation.

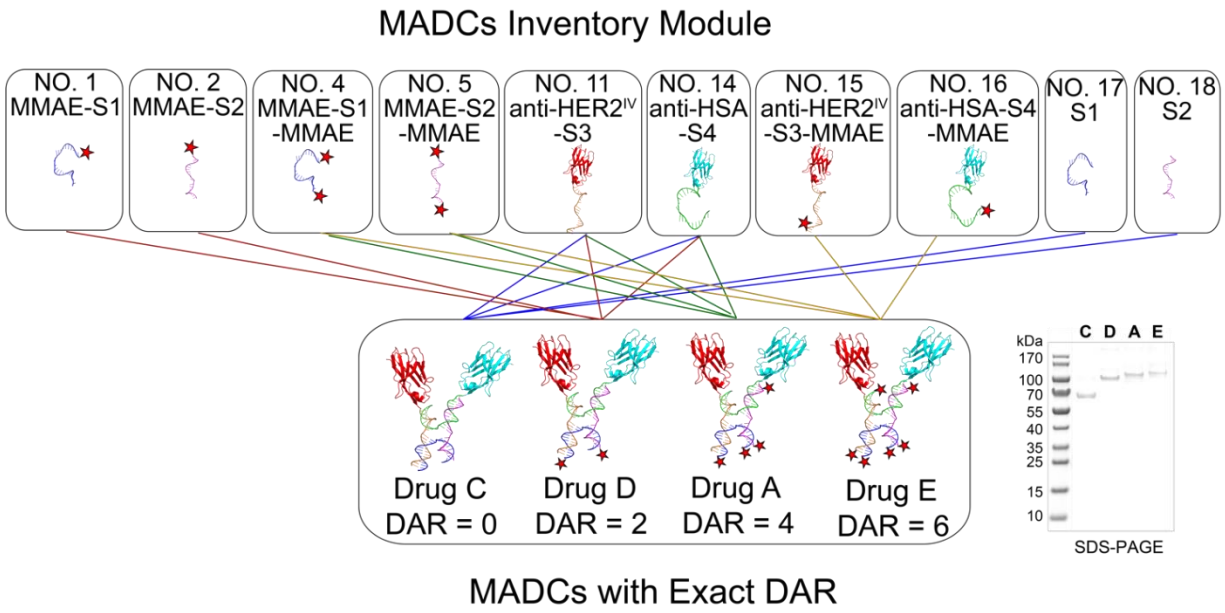

Figure S7. Anti-HER2 MADCs with different DAR were assembled with several basic units from MADCs inventory, and the drug quality was assessed with SDS-PAGE gel.

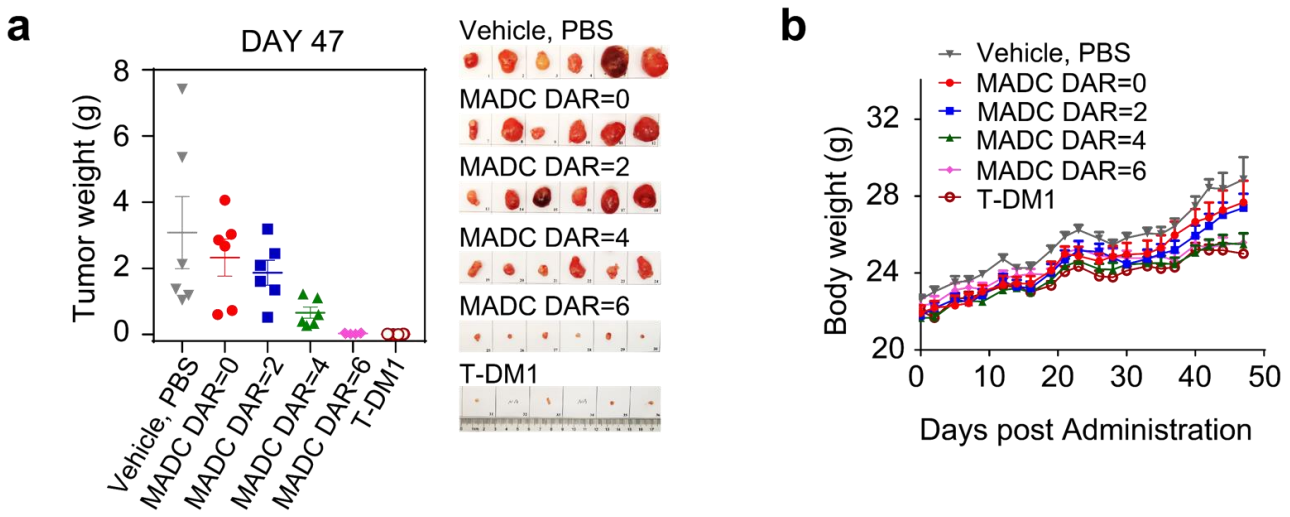

Figure S8. Monitoring of the tumor and body weights for MADCs treatment with different DAR in the HER2$^+$ HCC1954 murine xenograft model. HCC1954 cells were implanted subcutaneously into BALB/c nude mice (*n* = 6 per group) and treated by intravenous injection with MADCs with DARs from 0 to 6 as well as PBS and T-DM1. Tumor was weighed at day 47 post MADCs, T-DM1 or PBS injection (**a**) and body weights were monitored 4 times per week during treatment (**b**).

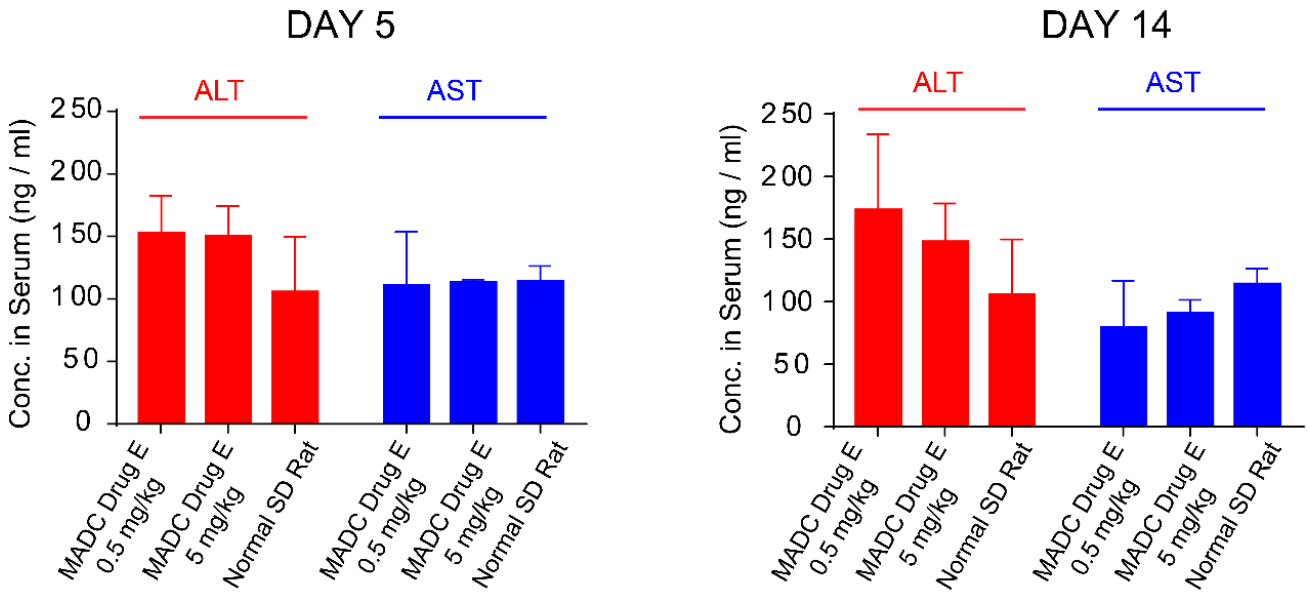

Figure S9. Serological examination of potential hepatotoxicity of MADC Drug E (Table S2) of DAR = 6. Serum samples were collected from each group at Day 5 and Day 14 after the injection of Drug E with dosage of 0.5 and 5 mg/kg. AST and ALT levels were examined by ELISA in duplicate, and mean value was calculated from AST and ALT levels in three mice of each group (n = 3).

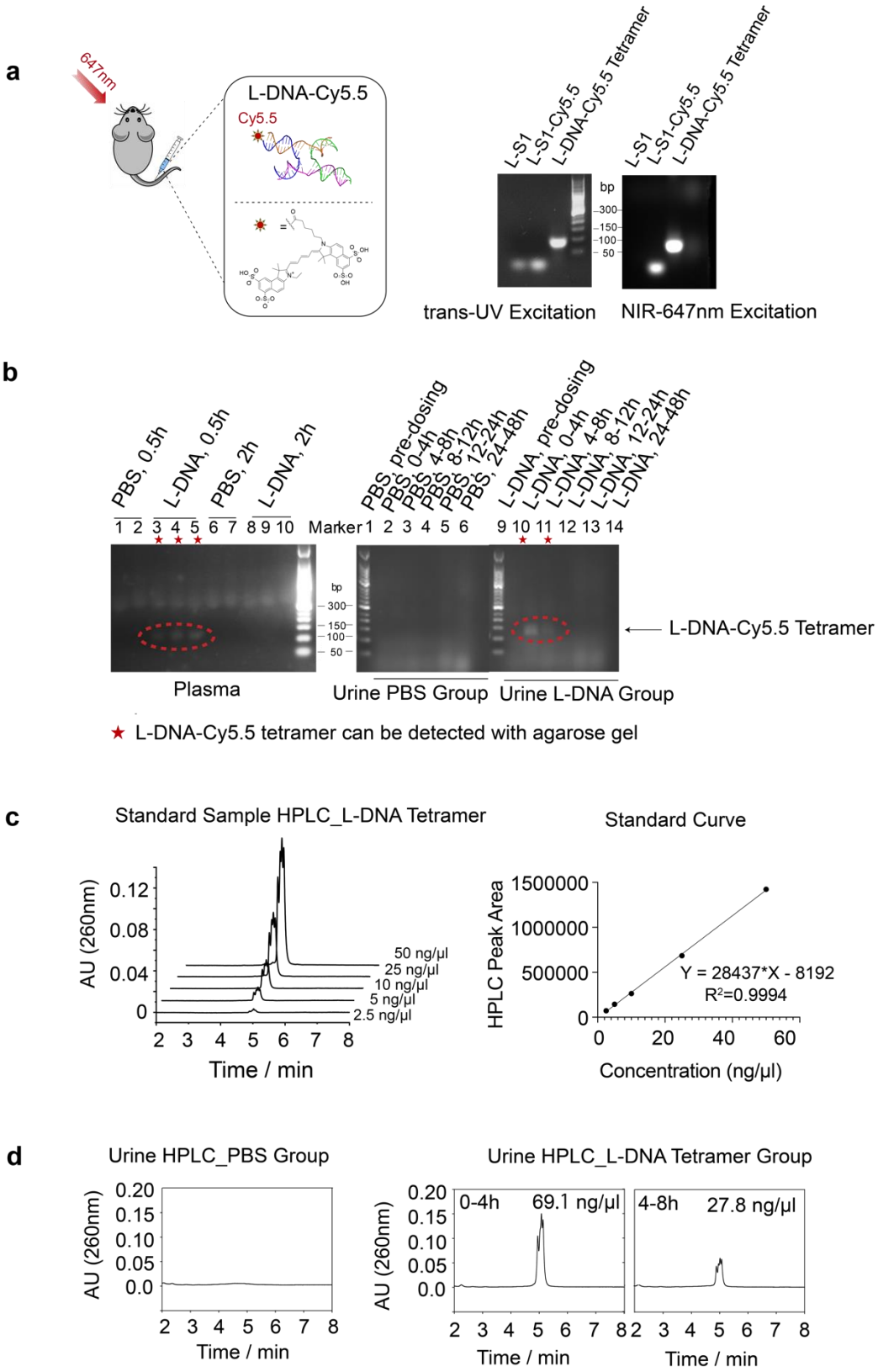

Figure S10. L-DNA tetramer detection in mice plasma and urine. (**a**) L-DNA-Cy5.5 tetramer was prepared by conjugating the S1 with the fluorescent probe Cy5.5 at the 5' end (left). The assembled L-DNA-Cy5.5 tetramer was characterized on agarose gel using trans-UV excitation and NIR-647nm

excitation (right). (**b**) BALB/c mice were injected intravenously with L-DNA-Cy5.5 tetramer (2.6 mg/kg) and PBS (vehicle). Plasma and urine were collected at different time points as indicated by the lane labeling. For the plasma sample, methanol was added to the sample at 1:1 v/v, followed by mixing and centriguation to remove protein aggregates. Then, 10 µL aliquot of supernatant was loaded to agarose gel for characterization (*left*). For the urine sample, 10 µL was directly loaded to agarose gel for characterization (*right*). * indicate the timepoints at which L-DNA-Cy5.5 tetramer can be detected on the agarose gel.

(**c**) L-DNA tetramer standard samples with a range of known concentrations (2.5, 5, 10, 25, 50 ng/µl) were injected to a Thermo DNA PacRP column and analyzed with the Waters ACQUITY® UPLC system. The L-DNA tetramer elution time is 4.86-5.26 min according to the 260 nm UV absorbance (left). By calculating the peak areas, a concentration vs. peak area calibration plot was generated for the column (right).

(**d**) Analysis of urine samples (10 µL) from the PBS and L-DNA tetramer groups as in (c). While the L-DNA group clearly showed elution peaks for the 0-4h and 4-8h time points, no elution peaks were observed for the PBS group. Using the established calibration curve in (c), the L-DNA tetramer concentration in urine were estimated to be around 69.1 and 27.8 ng/µl, respectively, for the 0-4h and 4-8h time points.

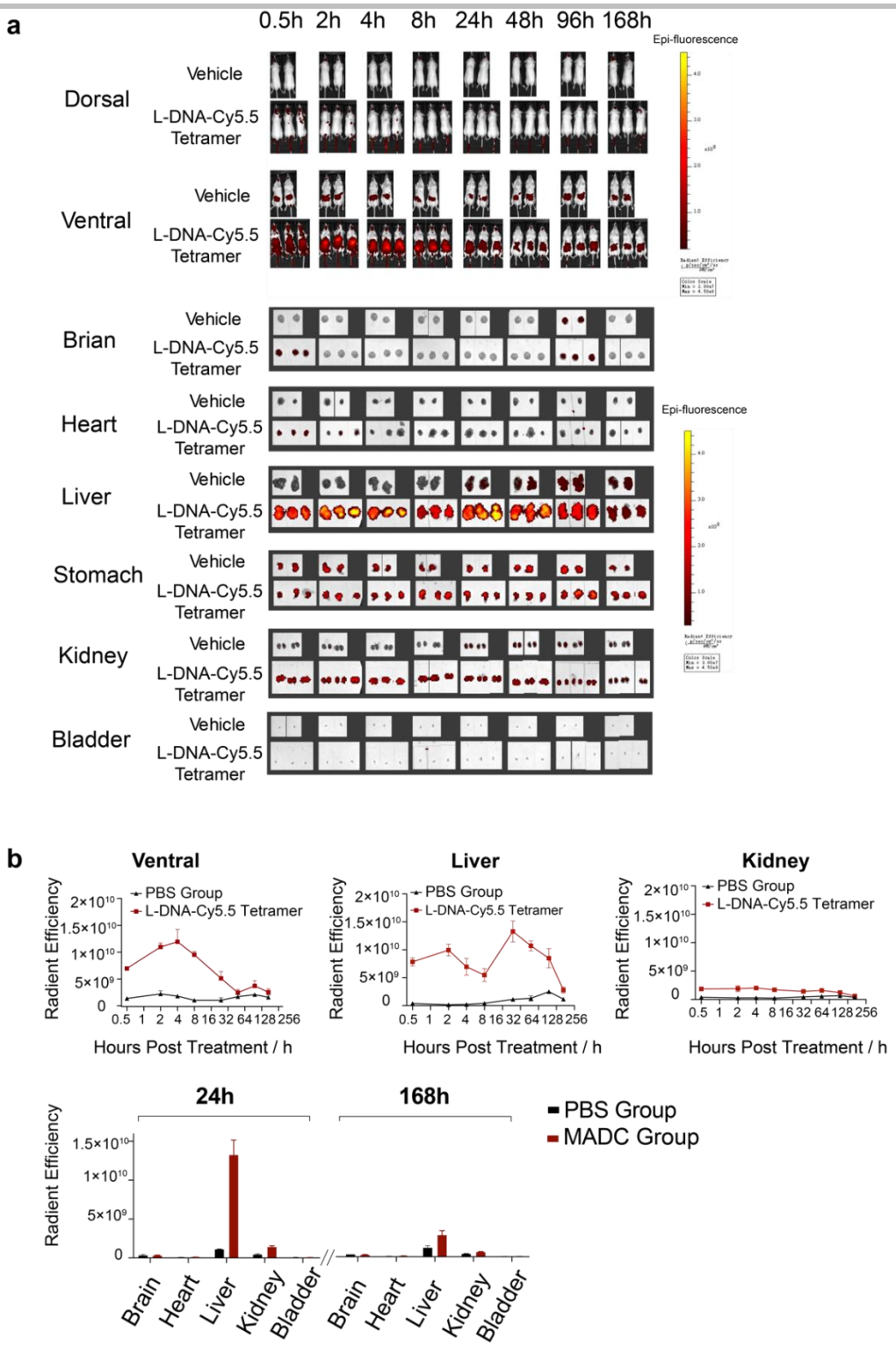

Figure S11. Systemic distribution of L-DNA-Cy5.5 tetramer in vivo. (**a**) Fluorescent images of mice injected intravenously with L-DNA-Cy5.5 tetramer (2.6 mg/kg) or PBS (vehicle) at eight different time points (0.5, 2, 4, 8, 24, 48, 96, and 168 hours). Six tissues (brain, heart, liver, stomach, kidney, bladder) were collected and imaged at different time points. (**b**) Plots of fluorescence intensity of ventral body, liver and kidney at different timepoints. The fluorescence were quantified by a small animal imager (PerkinElmer IVIS Kinetic III) and represented graphically as radiant efficiency (photons s^{-1} cm^{-2} per str)/(μW cm^{-2}) (upper panel). Biodistribution in different tissues at 24h and 168h post injection (p.i.) of L-DNA-Cy5.5 tetramer (lower panel). Stomach was excluded due to strong fluorescence background in PBS group.

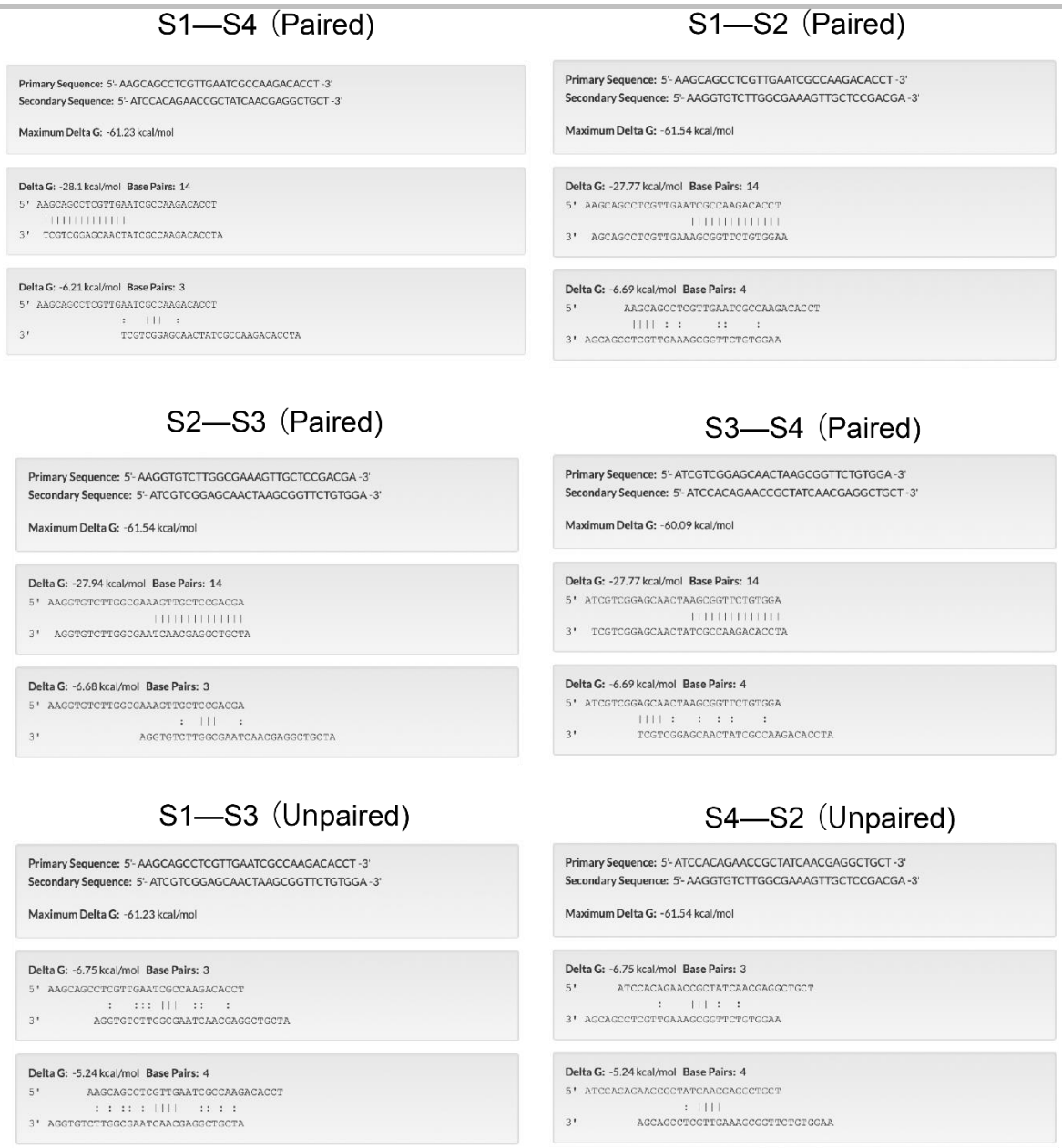

Fig. S12. Analysis of hetero-dimerization between two sequences among S1-S4 using the IDT oligo analyzer. The free energy of wanted pairing are less than -27 kcal/mol and unwanted pairing are more than -7 kcal/mol.

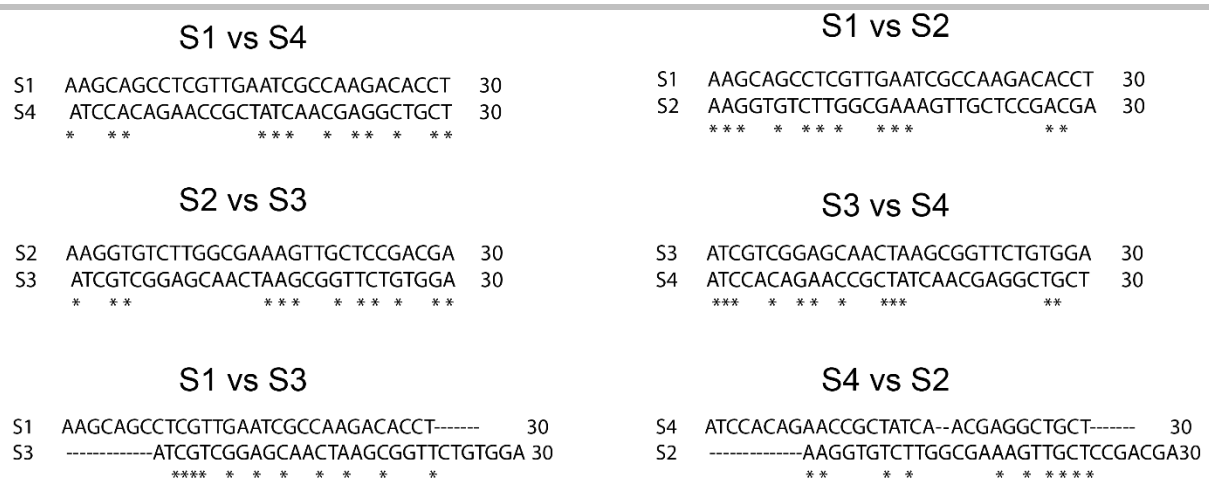

Figure S13. DNA sequence alignment with Clustal Omega. Invariant DNA bases are indicated by *.

SUPPORTING INFORMATION

References

[1] Jr. J. SantaLucia; D. Hicks, *Annu. Rev. Biophys. Biomol. Struct.* **2004**, 33, 415-40.
[2] M. Hilde Adi Pierrette Revets, W. Carlo Boutton, M. Hendricus Renerus Jacobus Mattheus Hoogenboom, US Patent 8975382-B2, **2015**.
[3] B. Els Anna Alice Beirnaert, M. Hilde Adi Pierrette Meise, M. Hendricus Renerus Jacobus Mattheus Hoogenboon, H. Heidi Maria Florence Jonckheere, S. Torsten Dreier, US Patent 2010113339, **2010**.
[4] L. Pan, C. Cao, C. Run, L. Zhou, J. J. Chou, *Adv. Sci. (Weinh)* **2020**, *7*, 1900973.